Nanoscale

Accepted Manuscript

This article can be cited before page numbers have been issued, to do this please use: J. Bizeau, J. Journaux-Duclos, C. Kiefer, B. Freis, D. Ihiawakrim, M. D. L. A. Ramirez, T. Lucante, K. Parkhomenko, C. Vichery, J. Carrey, O. Sandre, C. Bertagnolli, O. Ersen, S. Begin-Colin, V. Gigoux and D. Mertz, *Nanoscale*, 2024, DOI: 10.1039/D4NR01388C.

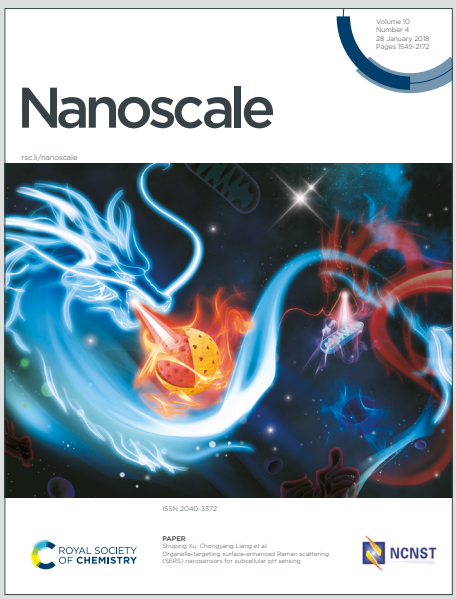

ROYAL SOCIETY OF CHEMISTRY

rsc.li/nanoscale

View Article Online
DOI: 10.1039/D4NR01388C

“Data for this article are available at Recherche.Data.Gouv repository at the URL : https://doi.org/10.57745/SVCWSI"

Tailoring the Pore Structure of Iron Oxide Core@Stellate Mesoporous Silica Shell Nanocomposites: Effects on MRI and Magnetic Hyperthermia Properties and Applicability to Anti-Cancer Therapies

Joëlle Bizeau[1], Justine Journaux-Duclos[2], Céline Kiefer[1], Barbara Freis[1], Dris Ihiawakrim[1], Maria de los Angeles Ramirez[1], Théo Lucante[1], Ksenia Parkhomenko[3], Charlotte Vichery[4], Julian Carrey[5], Olivier Sandre[6], Caroline Bertagnolli[7], Ovidiu Ersen[1], Sylvie Bégin-Colin[1], Véronique Gigoux[2], Damien Mertz[1]

[1] Institut de Physique et Chimie des Matériaux de Strasbourg (IPCMS), UMR-7504 CNRS-Université de Strasbourg, 23 rue du Lœss, BP 34 67034, Strasbourg Cedex 2, France.

[2] Centre de Recherches en Cancérologie de Toulouse UMR1037 CNRS - Inserm/Université Paul Sabatier, 1 avenue Jean Poulhes, BP 84225, 31432 Toulouse, Cedex 4, France.

[3] Institut de Chimie des Procédés pour l'Energie, l'Environnement et la Santé (ICPEES), UMR-7515 CNRS-Université de Strasbourg, 25 rue Becquerel, 67087 Strasbourg, France

[4] Université Clermont Auvergne, Clermont Auvergne INP, CNRS, ICCF, F-63000 Clermont-Ferrand, France

[5] LPCNO (Laboratoire de Physique et Chimie des Nano-Objets), Université de Toulouse, CNRS, INSA, UPS, 31077 Toulouse, France

[6] Laboratoire de Chimie des Polymères Organiques (LCPO) UMR 5629 Univ. Bordeaux / CNRS / Bordeaux INP, 16 Avenue Pey-Berland, 33607 Pessac France

[7] Institut Pluridisciplinaire Hubert Curien (IPHC), UMR 7178 CNRS-Université de Strasbourg, 25 Rue Becquerel, 67087 Strasbourg, France

Abstract

Core-shell nanocomposites made of iron oxide core (IO NPs) coated with mesoporous silica (MS) shells are great promising theranostic agents. While the core is being used as an efficient heating nanoagent under alternating magnetic field (AMF) and near infra-red (NIR) light and as a suitable contrast agent for magnetic

View Article Online
DOI: 10.1039/D4NR01388C

resonance imaging (MRI), the MS shell is particularly relevant to ensure colloidal stability in a biological buffer and to transport a variety of therapeutics. However, a main challenge with such inorganic nanostructures is the design of adjustable silica structures especially with tunable large pore which would be useful for instance for the delivery of large therapeutic biomolecules loading and further sustained release. Further, the effect of tailoring porous silica structure on the magneto or photothermal dissipation still remains poorly investigated. In this work, we address a deep investigation of the growth of stellate mesoporous silica (STMS) shell around IO NPs cores and of its micro/mesoporous features respectively through time-lapse and *in situ* liquid phase transmission electron microscopy (LPTEM) and detailed nitrogen isotherm adsorptions studies. We found here that the STMS shell features (thickness, pore size, surface area) can be finely tuned by simply controlling the sol-gel reaction time affording a novel range of IO@STMS core@shell NPs. Finally, regarding the responses under alternating magnetic fields and NIR light which are evaluated as function of the silica structure, IO@STMS NPs having tunable silica shell structure are shown to be efficient as T_2-weighed MRI agents and as heating agents for magneto and photo-induced hyperthermia. Further, such IO@STMS are found to display anti-cancer effects in pancreatic cancer cells under magnetic fields (both alternating and rotating).

Keywords: Stellate mesoporous silica, Iron oxide nanoparticles, Core-shell nanoparticles, Anti-cancer application, Magnetic hyperthermia, MRI.

View Article Online
DOI: 10.1039/D4NR01388C

I. Introduction

Nowadays, a true challenge in the field of nanomedicine is the development of multifunctional materials that could be used to perform imaging, drug delivery and other innovative therapies using a single platform, allowing the reduction of side effects and the improvement of diagnosis and therapeutic efficiency[1,2]. Among the potential materials, core-shell iron oxide@silica nanoparticles (IO@silica NPs) are particularly interesting systems as the association of these two materials naturally combine several advantageous properties. Indeed, IO NPs are already commercially used for Magnetic Resonance Imaging (MRI) as they are very good T_2 contrast agents[3–6]. In addition, they are recognised as efficient heating agents under alternating magnetic field (AMF) stimulus[3,7–10] and their potential as heating agents by Near-InfraRed (NIR) light irradiation is also emerging[11–14]. Last but not least, IO NPs are known to have a low toxicity and to be well internalised and degraded by cells[3,4], which given all these features, make them great potential particles for theranostic applications. However, without a robust and efficient coating strategy, they suffer from a rapid blood capillary agglomeration and elimination, reducing their efficiency[15,16]. Among different coating possibilities (polymers, dendrimers, specific biomolecules, silica[16]), synthesising a porous silica (MS) shell around the IO NPs presents some interesting features. Indeed, the size and shape of silica nanomaterials are tunable, the surface chemistry is versatile and very importantly, it is recognised a generally safe material by the FDA[17–19]. Furthermore, MS NPs are reported to degrade *in vitro* and *in vivo* and its main dissolution product, silicic acid, is reported to be water soluble and non-toxic. Thus, the addition of a MS layer coating to IO NPs is very appealing for medical applications, especially for drug delivery[20–24].

Such MS shell coatings around IO NPs[20,21,25,26,] but also other inorganic NPs[27–30] were usually synthesised using surfactant templating, with the most famous one being cetyltrimethylammonium bromide (CTAB). The control of the shell thickness is one of the crucial features of such synthesis and it is mainly achieved by the amount of reactants, as notably shown by Ye *et al*. with the molar ratio [CTAB]/[Fe_3O_4][31]. Recently, there have been a tremendous interest tuning the pore size, especially to tailor large pore around IO cores. Indeed, the use of CTAB leads to pore size of ~3 nm, which is enough for the delivery of small drugs, but the delivery of larger

View Article Online
DOI: 10.1039/D4NR01388C

molecules such as proteins, RNA or DNA has gained a growing interest these last years[32].

Despite that small pore MS coatings with adjustable shell thicknesses were already reported around superparamagnetic IO NPs (size in the range 10-25 nm), the tailoring of porous silica structure and tuned increase of pore size around such NPs remained quite limited. In some approach, elegant pore size tuning was achieved using swelling micelle method which however limits the range of pore size at *ca*. 3 - 6 nm[33]. Very recently, interesting works have described the tunable design of MS shells having radially oriented pores around a magnetic core through the so-called interfacial co-assembly in bi-liquid phase where addition of a water non-miscible apolar solvent was used as a way to expand/tune pore size[34]. These works were nevertheless essentially focused on bigger controlled iron oxide-clusters (*ca*. up to hundreds of nms)[35–38]. For instance, by investigating different synthesis parameters (surfactant concentration, amount of organic solvent, or silica precursor, reaction temperature, reaction time, etc..), Nemec and Kralj have developed versatile silica-shell morphologies around wide range of magnetic inorganic cores, having hierarchical dual pore sizes from ~3 to ~40 nm, with centre-radial and raspberry-like pore geometries[36]. In another work, Fiedler *et al*.[38] have developed a powerful approach for synthesizing different silica shells of various thicknesses and porosities in the range *ca*. 5-10 nm that can be adjusted independently around IO cluster cores of various sizes, especially by changing the composition of the cyclohexane/TEOS phase.

As addressed in this present article, the pore increase can also be obtained by another method adapted from K. Zhang *et al*.[39] where CTA^+, counterion tosylate (CTATos) is used to orient the silica structure towards stellate mesoporous silica STMS having pore size of *ca*. 10-15 nm. Previously in our team, we synthesized and developed core free STMS and core@shell IO@STMS (where IO NPs are made by thermal decomposition) for biological and environmental applications[40–43] and the IO@STMS NPs were notably shown to be suitable systems for MRI, MHT and PHT[44–46]. However, these IO@STMS core-shell nanostructures have been synthesised only at a given final core-shell size (*ca*. 120 nm) and to date, no work has reported in depth the growth mechanism of the STMS shell around IO NPs cores or the possibilities to design IO@STMS NPs having tailored shell structure and its

View Article Online
DOI: 10.1039/D4NR01388C

resulting properties for nanomedicine applications (textural pore structure, colloidal stability, response under magnetic fields or NIR light…).

Hence to the best of our knowledge, there is no report that makes use of CTATos as porogen surfactant combined with the controlled sol-gel reaction time applied around *ca*. 25 nm size iron oxide NPs (synthesized by thermal decomposition) to generate individual core@shell with tunable growth and pore structure (from 7 to 16 nm). Worthy to note is in all the previous mentioned reports, no investigation of the silica pore structure effects on magneto and photothermal dissipation and MRI properties was reported and approaches based on the visualisation in real-time through *in situ* Liquid Phase TEM (LPTEM) method of the silica growth were not yet proposed.

In this work, we report the great control of the stellate mesoporous silica shell growth around these IO NPs, to afford range of IO@STMS core-shell NPs designed with tunable silica shell. First, with the aim to evidence the silica shell growth with reaction time around IO NPs core, we investigated the growth kinetic of STMS shell by a time-lapse TEM imaging of the NPs taken out at different time-points of the synthesis and by performing *in situ* LPTEM imaging to get direct observation of the STMS shell growth. Then, using different synthesis times corresponding to different shell growths, denoted IO@STMS-t (t=40, 60, 120 min, growth time) we deeply investigated the textural pore size properties (microporosity, mesoporosity) and the colloidal stability of these tunable core-shell NPs. We then evaluated the responses of the different IO@STMS-t NPs under external fields (magnetic field and NIR light) and the effects of pore structure or shell thickness were discussed. Hence, their potential as T_2 contrast agents was evaluated for MRI by measurements of their relaxivities and their potential as good heating agents for MHT and PHT was evaluated by Specific Absorption Rate (SAR, $W.g^{-1}$) measurements. At last, the potential use of such IO@STMS-t NPs for anti-cancer application was evaluated by investigating their cytotoxicity towards the pancreatic cancer cell line MiaPaca2 in presence and absence of magnetic field stimuli (alternating and rotating). The main concept of this work is represented in **Scheme 1**.

View Article Online
DOI: 10.1039/D4NR01388C

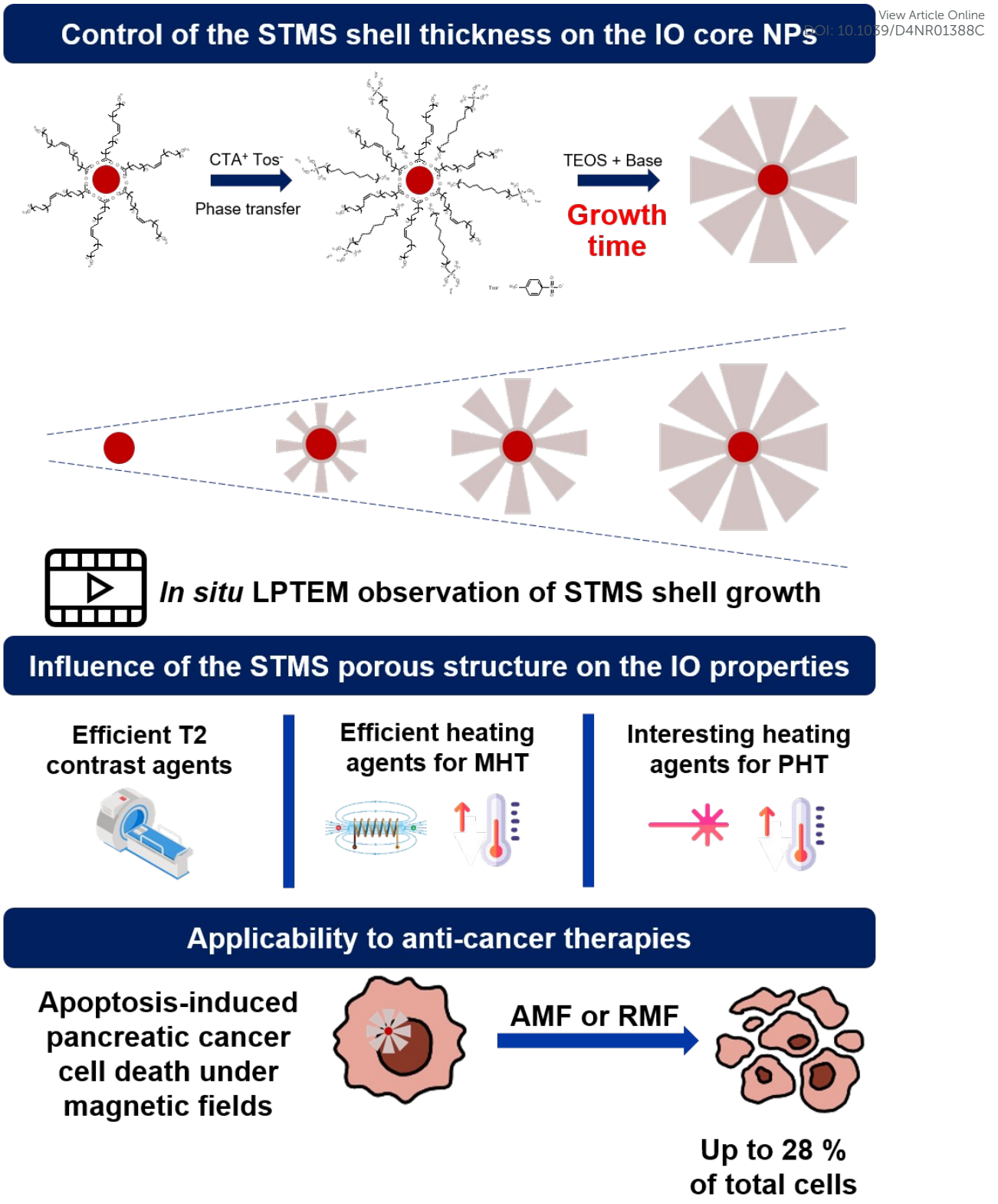

Scheme 1: Representative scheme of the study.

View Article Online
DOI: 10.1039/D4NR01388C

II. Materials and methods

II.1 Materials

All materials were used as provided. Anhydrous absolute ethanol (EtOH, CAS 64-17-5), chloroform ($CHCl_3$, CAS 67-66-3), nitric acid 65 % (HNO_3, CAS 7697-37-2), acetone (C_3H_6O, CAS 67-64-1) were purchased from Carlo Erba Reagents. Dibenzylether (DBE, CAS $C_{14}H_{14}O$, CAS 103-50-4) and squalane ($C_{30}H_{62}$, CAS 111-01-3) were purchased from Acros Organics. Cetyltrimethylammonium p-toluene sulfonate (CTATos, CAS 138-32-9) and Trizma ® base (AHMPD, CAS 77-86-1) were pruchased from Sigma life science. Tetraethylorthosilicate (TEOS, CAS 78-10-4) was purchased from Aldrich chemistry, oleic acid ($C_{18}H_{34}O_2$, CAS 112-80-1) from Alfa aesar, ferric chloride ($FeCl_3$, CAS 7705-08-0) from Sigma Aldrich, PBS from Sigma and sodium stearate ($C_{18}H_{35}NaO_2$, CAS 822-16-2) from TCI. Iron and indium (115In) plasma emission standards, 1 $g.L^{-1}$, were purchased from AccuStandard.

For *in vitro* experiments, dimethylsulfoxide (DMSO, C_2H_6SO, CAS 67-68-5) and 3-(4,5-dimethylthiazolyl-2)-2,5-diphenyltetrazolium bromide (MTT, $C_{18}H_{16}BrN_5S$, CAS 298-93-1) were purchased from Sigma, Penicillin-Streptomycin (P4333) was purchased from Sigma-Aldrich. Dulbecco's Modified Eagle Medium (DMEM GlutaMAX™) and phosphate-buffered saline (PBS) were purchased from Life technologies. Foetal bovine serum (FBS) was purchased from Eurobio scientific.

II.2 Synthesis of IO NPs

Thermal decomposition was used to synthesise oleic acid-stabilised iron oxide nanospheres with a mean diameter of around 20 nm following a recently reported procedure[47]. Briefly, iron stearate (III) was prepared by precipitation of sodium stearate and ferric chloride salts in an aqueous solution as described[48]. Then, 1.85 g (2 mmol) of the synthesised iron(III) stearate was mixed with 1.89 g of oleic acid (6.7 mmol) in a two-neck round-bottom flask in 19.5 mL (15.8 g) of squalane and 0.5 mL (0.53 g) of DBE. The mixture was heated at 120 °C and kept at this temperature for 60 min. The condenser was then connected to the flask and the solution was heated to 330 °C prior to be kept under reflux for 60 min under air. After cooling to room temperature, the viscous suspension was solubilised in 10 mL of chloroform. The NPs were precipitated by addition of an excess of acetone and washed three times

View Article Online
DOI: 10.1039/D4NR01388C

with chloroform and acetone (ratio 1:4, centrifugation 14,000 g, 5 min). The NPs were then redispersed in chloroform and stored until further use.

II.3 Resuspension of IO NPs in deionised water

For some characterisation, oleic-acid coated IO NPs were further coated with CTA+ surfactant with the aim to be re-dispersed in deionised water (dH_2O). To do so, 19.2 mg of CTATos were dissolved in 2 mL of dH_2O at 50 °C under stirring in a 5 mL glass vial. Then, the stirring was increased to 950 rpm and 488 µL of the IO solution at

4.1 $mgFe.mL^{-1}$ in chloroform was added to the vial. The temperature was then increased to 65 °C and the solution kept under this vigorous stirring until full evaporation of chloroform. The final solution was a 1 $mgFe.mL^{-1}$ IO NPs colloidal solution in dH_2O.

II.4 Synthesis of IO@STMS-t NPs

This procedure is described for IO NPs of 26.6±2.1 nm. The volume of IO NPs solution is adapted in function of the IO NPs diameter. The protocol was used as described previously[44–46] with some standardisations. In a 50 mL round bottom flask, 240 mg of CTATos was dissolved in 25 mL of dH_2O at 50 °C (oil bath) under stirring (300 rpm). Then, 27.6 mg of AHMPD pH buffer salt was added and dissolved. The stirring was then increased to high speed (950 rpm) prior to the addition of the adequate volume of IO NPs in chloroform (31.91 mg, corresponding here to 7 mL). The oil bath temperature was increased to 65 °C to evaporate the chloroform. The mixture changed from hazy grey after addition of the IO NPs to limpid dark black after the evaporation of chloroform. The mixture was left under stirring ten additional minutes to be sure that all the chloroform was evaporated before increasing the temperature to 70 °C. Once the temperature of the oil bath was stabilised, the mixture was left under stirring for 30 min to let its temperature stabilise too, prior to the addition of 1.5 mL of TEOS drop by drop for one min. The stirring was then reduced to 750 rpm and left for reaction.

View Article Online
DOI: 10.1039/D4NR01388C

For the kinetic study, a sample was collected at 5 – 10 – 20 – 30 – 40 – 50 – 60 – 90 – 120 min, quickly cooled with an ice bath and washed twice with EtOH (15,000 g, 10 min). Without kinetic study, the reaction was left for 40 – 60 – 90 and 120 min.

After reaction, the NPs were collected by centrifugation (12,000 g, 20 min) and washed twice with 15 mL of EtOH (12,000 g, 12 min). The CTATos was then extracted by dispersing the NPs in 20 mL of NH_4NO_3 (20 mg.mL^{-1} in EtOH) and heated at 70 °C under stirring. The extraction was then followed by two washings with 15 mL of dH_2O and two washings with 15 mL of EtOH (12,000 g, 12 min). The extraction status was followed by zeta potential in dH_2O as it was positive before extraction (~ 30 mV) and became negative when all the CTATos was extracted (~ -20 mV). Here, a first extraction was performed for one night and a second for 1 h. The zeta potential was then stable, meaning that all the CTATos was removed. The NPs were then resuspended in EtOH prior to be used.

The particles were washed three times with dH_2O prior to be used for MRI, MHT or PHT properties evaluation. Particles were designated as IO@STMS-t with t being the STMS growth time.

II.5 *In vitro* biological experiments

II.5.1 Cell culture

The pancreatic cancer cell line MiaPaca2 was cultured in complete DMEM medium containing 10 % FBS, 100 IU.mL^{-1} penicillin/streptomycin in a humidified atmosphere at 95 % air and 5 % CO_2 at 37 °C. Such DMEM/FBS/penicillin/streptomycin medium is designated as “cell culture medium” for the following protocols.

II.5.2 Cytotoxicity

An average of 10^4 cells/well were seeded in a 96-well plate, grown overnight, and incubated with increased concentrations of IO@STMS-t NPs (from 0 to 100 µgFe.mL^{-1}) in cell culture medium for 24, 48 or 72 h. The cells maintained in the incubation medium without NPs served as controls. Cell viability was then quantified using the MTT assay. The experiment was performed in quintuplicate.

View Article Online
DOI: 10.1039/D4NR01388C

Prior to be used, the NPs (80 µL) were washed once with dH_2O prior to be resuspended in cell culture medium (centrifugation 12,000 rpm, 10 min).

II.5.3 Cellular uptake

An average of 3×10^5 MiaPaca2 cells were seeded onto 35 mm dishes in cell culture medium. Cells were incubated with nanoparticles at 0, 0.5 or 5 µgFe.mL^{-1} in cell culture medium for 72 h, at 37 °C in a 5 % CO_2 atmosphere, washed twice with ice-cold PBS, and centrifuged (1,500 rpm, 10 min). The amount of internalised IO NPs was determined through ICP-MS titration of Fe after acidic digestion of the cell pellets in concentrated HNO_3 for 12 h. The results were expressed in pg of iron per cell and in percentage of initial mass of iron internalised. The experiment was performed in quadruplicate. Prior to be used, the NPs (5 µL) were centrifuged and resuspended in dH_2O (centrifugation 12,000 rpm, 10 min).

II.5.4 Cytotoxicity under magnetic stimulus: high frequency alternating (AMF) or low frequency rotating (RMF) magnetic field

An average of 25×10^3 MiaPaca2 cells/compartment were seeded onto four-compartments Cellview™ dishes (Greiner Bio-One) and grown overnight in cell culture medium prior to be incubated with IO@STMS-t NPs at 0, 0.5 or 5 µgFe.mL^{-1} for 72 h at 37 °C. The cells were then washed with cell culture medium and exposed, or not, to AMF (f=250 kHz, H=20 mT (16 kA.m^{-1})) or to RMF (f=1 Hz, H=40 mT (32 kA.m^{-1})) for 2 h. The temperature was strictly maintained at 37 °C and controlled using a thermal optical fibre probe (Reflex, Neoptix, Quebec City, QC, Canada) placed in the incubation medium during the magnetic field exposure. At the end of the experiment, the cells were placed in a humidified atmosphere at 5 % CO_2 at 37 °C for further analyses. The cell death was then analysed by Annexin V / Propidium Iodide labelling. The experiment was performed in quadruplicate. Prior to be used, the NPs (5 µL) were centrifuged and resuspended in dH_2O (centrifugation 12,000 rpm, 10 min).

View Article Online
DOI: 10.1039/D4NR01388C

II.5.5 Cytotoxicity under multiple magnetic stimuli: high frequency alternating (AMF) or low frequency rotating (RMF) magnetic field

An average of 10^4 MiaPaca2 cells/compartment were seeded onto four-compartments Cellview^{TM} dishes (Greiner Bio-One) and grown overnight in cell culture medium prior to be incubated or not with IO@STMS-40 NPs at 5 µgFe.mL^{-1} for 72 h at 37 °C. The cells were then washed twice with cell culture medium and exposed to AMF (f=250 kHz, H=20 mT (16 kA.m^{-1})) or to RMF (f=1 Hz, H=40 mT (32 kA.m^{-1})) for 2 h every 24 h, for 3 days. The temperature was strictly maintained at 37 °C and controlled using a thermal optical fibre probe (Reflex, Neoptix, Quebec City, QC, Canada) placed in the incubation medium during the magnetic field exposure. The effects of magnetic field treatments were investigated on cell viability by counting the cell number using a cell counter (Beckman cell counter z2) 24 h after the last exposure. Thus, cells were seeded on day 1, incubated with particles from day 2 to day 4, then sample 1 was exposed to nothing, AMF or RMF on day 5 and cells were counted on day 6. Sample 2 was exposed to nothing, AMF or RMF on day 5 and 6 and cells were counted on day 7. Same process for sample 3 which was exposed three times to nothing, AMF or RMF: cells were counted on day 8. For the sake of clarity, a scheme is presented in the Results and Discussion section.

II.6 Characterisation methods

II.6.1 Transmission electron microscopy (TEM) and energy-dispersive X-ray analysis (EDX)

The TEM imaging of IO and IO@STMS-t NPs was performed with a JEOL 2100 TEM instrument operating at 200 kV after deposition of the particles on carbon-coated copper grids. The JEOL Si(Li) EDX detector was used to determine the mass of Si and Fe atoms. The open source software ImageJ was used to analyse the images and to determine the size distribution of the NPs.

In vitro samples were imaged using a Hitachi HU12A (Japan) TEM instrument operating at 75 kV. After their incubation with IO@STMS-t NPs (t=40, 60, 120) at 5 µgFe.mL^{-1} for 72 h, the cells were washed with PBS and fixed with 4 % glutaraldehyde in Sorensen buffer for 4 h at 4 °C. After washes, cells were post-fixed

View Article Online
DOI: 10.1039/D4NR01388C

in 1 % osmium tetraoxide (osmium 2 %, saccharose 0.25 mol.L^{-1}, Sorensen 0.05 mol.L^{-1}) for 1 h at 20 °C, followed by washings with distilled water and uranyl acetate 2 % for 12 h at 4 °C. After dehydratation, 70 nm sections of cells embedded in EMBed 812 resin were stained with uranyl acetate and lead citrate. The samples could then be imaged.

II.6.2 *In situ* Liquid Phase TEM (LPTEM)

In situ LPTEM was performed on a JEOL 2100F/Cs (S)TEM operating in continuous capture mode.

For these experiments, a Protochips liquid cell holder (Poseidon Select 510) was used for the in situ LPTEM analyses. The liquid cell holder contained a removable microchip composed of two Si_3N_4 membranes that isolated the liquid sample from the ultrahigh vacuum from the TEM column. The dimensions of the E-chip used in this work were 2 × 2 mm^2 or 6 × 4.5 mm^2. The thickness of the Si_3N_4 membranes was 50 nm, and the space between each membrane was 150 nm. The two microchips were washed in HPLC-grade acetone for ~ 2 min to remove a protective film and then washed with ethanol for 2 min to clean the Si_3N_4 membranes and they were submitted to plasma cleaning with an Ar/O_2 mixture for 30 s.

One of the microchips was placed on the *in situ* holder where a volume of 1 µL of the IO NPs was added. The second chip was then positioned on top to seal the liquid system (see **Figure S1** for a schematic representation). The sample holder containing the NPs was inserted into the microscope and TEOS was added by flow. Images were recorded using the AXON studio software with the Poseidon liquid-heating detector. Images were exported from AXON studio and analysed with ImageJ.

II.6.3 X-ray diffraction (XRD)

XRD patterns were collected with a Brucker D8 Discover diffractometer in Bragg Brentano geometry equipped with a monochromatic copper radiation source and an energy-resolved Lynx-eye XE-T detector in the 20-70° (2θ) range with a scan step of 0.03°. The measurements were performed at room temperature and high-purity silicon powder was used as an internal standard.

View Article Online
DOI: 10.1039/D4NR01388C

II.6.4 Dynamic Light Scattering (DLS) and Zeta Potential

DLS and Zeta potential were performed on a Zetasizer Nano-ZS (Malvern instruments). DLS measurements were recorded in triplicate at 25 °C and at a scattering angle of 173 ° using a 1 cm length plastic cell. The measurements were conducted with a concentration of 0.2 $mg.mL^{-1}$ of NPs in dH_2O.

Zeta potential measurements were recorded in triplicate at 25 °C using a DTS1070 folded capillary cell. The measurements were conducted in dH_2O at a concentration of NPs of 0.2 $mg.mL^{-1}$ or in PBS buffer (pH 7.4) when checking the extraction of the CTATos.

II.6.5 Nitrogen Adsorption-Desorption measurements

The textural properties of the prepared samples were studied by nitrogen adsorption-desorption measurements at -196 °C. The nanoparticles were degassed under vacuum at ambient temperature (around 20 °C) for 3 h to desorb the moisture before analysis. Specific surface area was calculated by Brunauer-Emmet-Teller (BET) method. Pore volume and pore size distribution were determined using desorption branch by the Barrett-Joyner-Halenda (BJH) method which is well suited for mesopore analysis. Horvath-Kawazoe model was used for determining pore-size distribution in a micropore analysis from a single adsorption.

II.6.6 Iron titration

II.6.6.1 By NMR ^{1}H-relaxometry

T_1 relaxation time measurements were used to quantify the amount of iron in the NPs. To do so, 100 µL of the IO@STMS-t NPs was collected and dried. Then, 323 µL of HNO_3 (65 %) was used to completely dissolve the IO@STMS-t NPs. Some heating at 60 °C could be used to help this digestion step. The sample was diluted precisely in a 10 mL calibrated flask and the T_1 relaxation was measured. The amount of iron was determined using a calibration curve established by measuring the longitudinal relaxivity r_1 of a standard solution of iron (III) nitrate at 2 % of HNO_3 (calibration curve presented in **Figure S2**). The variation of the relaxation rates ($1/T_1$)

View Article Online
DOI: 10.1039/D4NR01388C

as a function of [Fe^{3+}] from 0 to 3.6 mmol.L^{-1} was plotted and used for the calculations.

II.6.6.2 By Inductively Coupled Plasma-Mass Spectrometry (ICP-MS)

The iron content on biological samples collected from the cellular uptake experiments were measured on Agilent 8900 ICP-MS Triple Quad instrument. First, the cells were resuspended in 500 µL of dH_2O in order to be transferred in a glass vial for their digestion with 323 µL of HNO_3 (65 %) for one night. The samples were then partially diluted in dH_2O, filtered with 0.45 µm sterile PES syringe filter, and then diluted to 10 mL using a calibrated flask. The amount of acid was then reduced for ICP-MS analysis by diluting 1.60 mL of sample to a final volume of 5 mL. Indium (10 ppb) was added as internal standard. Linear calibration functions were obtained (r^2 of ≥ 0.999) and are presented in **Figure S3**.

II.6.7 Relaxometry

A Bruker Minispec 60 working at a Larmor frequency of 60 MHz for proton (1.41 T) at 37 °C was used to measure longitudinal T_1 and transversal T_2 relaxation times of IO@STMS-t NPs. The longitudinal relaxivity r_1 and transverse relaxivity r_2 values were calculated according to the general equation of relaxivity given in **Eq. 1**:

$$R_i = R_i^0 + r_i \times [\text{IO@STMS}] \quad (\text{Eq. } 1)$$

where where R_i is the respectively longitudinal (i=1) or transverse (i=2) relaxation rate ($R_i=1/T_i$ in s^{-1}) in the presence of the NPs, R_i^0 the relaxation rate of the aqueous medium (in the absence of the NPs) and r_i the corresponding relaxivity value of the NPs (in $s^{-1}.mM^{-1}$). To perform this experiment, the particles were diluted at 4 – 2 – 1 – 0.5 – 0.25 mmolFe.L^{-1} in dH_2O.

II.6.8 Magnetothermal measurements

II.6.8.1 By AC magnetometry

View Article Online
DOI: 10.1039/D4NR01388C

The heating efficiency of IO@STMS-t NPs was measured by AC magnetometry using the AC Hyster™ setup from NanoTech Solutions with a pick-up coil technology[49]. To do so, 40 µL of aliquots of freshly sonicated suspensions of IO NPs in chloroform at 3.35 mgFe.mL^{-1} or of IO@STMS-t NPs in EtOH at 0.5 mgFe.mL^{-1} (thus
4.6 mgIO.mL^{-1} and 0.69 mgIO.mL^{-1} respectively) was introduced in 3 mm diameter 4 inches length NMR tubes (VWR, France). The magnetisation cycles M(H) were then measured three times with a delay of 45 s between each measurement at a frequency f of 280 kHz and an amplitude H of 20 kA.m^{-1}. Further measurements were performed some days later after sonication at 280 kHz or 217 kHz and 24 kA.m^{-1}. The measured cycles were averaged and normalised by the exact weight of IO present in the tube to get the mass magnetisation in A.m^2.kg^{-1}.

II.6.8.2 By calorimetry

The temperature profiles under AMF stimulus were performed using a D5 series instrument equipped with a G2 multi-mode 1500 W driver (Nanoscale Biomagnetics™, nB) and a CAL1 coil under MaNIaC™ software. Standard HPLC 1.5 mL vials well adapted for magnetothermal measurements were used and filled with 1 mL of IO-CTA+ or IO@STMS-t NPs at 0.5 mgFe.mL^{-1} in dH_2O. An AMF with a frequency f of
303.50 kHz and an amplitude H of 300 G (24 kA.m^{-1}) was applied and the temperature profiles were recorded for 5 min.

II.6.9 Photothermal measurements

The temperature profiles under NIR light irradiation were performed using an EA-PS 2042 10 B power supply coupled with a 1,064 nm wavelength laser beam generated by a CCMI apparatus from AeroDIODE™. The temperature was recorded using a temperature sensor. Briefly, 1 mL of IO-CTA$^+$ or IO@STMS NPs at 0.5 mgFe.mL^{-1} in dH_2O was added to a 1 cm path length plastic cell inserted in a closed CVH100-CV cell from Thorlabs. The laser was then applied with a power of 1.020 W and the temperature profiles recorded for 10 min.

View Article Online
DOI: 10.1039/D4NR01388C

II.6.10 Processing of the hyperthermia curve measurements to obtain the Specific Absorption Rate (SAR) and the Intrinsic Loss Power (ILP)

The SAR is calculated using different equations in function of the method used to measure the hyperthermia properties of the NPs. **Eq. 2** is used in the case of AC magnetometry[50]:

$$SAR\ (\mathrm{W.g^{-1}}) = \frac{\mu_0}{m_{\mathrm{IO}}} \times f \times \oint_{\mathrm{cycle}}^{T} M_t(H_t)\, dH_t \quad (Eq.2)$$

where μ_0 is the magnetic permeability of vacuum, m_{IO} is the mass of iron oxide in g (obtained as m_{IO}=1.38 x m_{Fe}) and $M_t(H_t)$ is the magnetization curve. While **Eq. 3** is used in the case of calorimetry (MHT and PHT):

$$SAR\ (\mathrm{W.g^{-1}}) = m_s \times \frac{C_s}{m_{IO}} \times \left[\frac{dT}{dt}\right]_{t=0} \quad (Eq.3)$$

where m_s and C_s are the mass in g and the heat capacity in J.kg^{-1}.K^{-1} of the solvent respectively, m_{IO} is the mass of iron oxide in g and (dT/dt)t=0 is the derivative function of the temperature at t=0. This term is determined by fitting the temperature curve with a second order polynomial function as described by Périgo *et al.*[50]. The mass of iron oxide is determined as m_{IO}=1.38 x m_{Fe} as calculated from the relative molar masses of Fe_3O_4 and Fe.

In order to compare the heating efficiency of NPs between different lab or studies, the ILP can be calculated following the **Eq. 4**:

$$ILP\ (\mathrm{nH.m^2.kg^{-1}}) = \frac{SAR \times 10^9}{f \times H^2} \quad (Eq.4)$$

where the SAR is in W.g^{-1}, f is the frequency of the magnetic field in kHz and H is the amplitude of the magnetic field in A.m^{-1}.

II.6.11 Magnetic measurements (VSM)

View Article Online
DOI: 10.1039/D4NR01388C

The magnetization curve of IO@STMS-t NPs was measured on a VSM magnetometer (PPMS, Quantum Design, USA) at room temperature. The samples were prepared by drying 5 µL of NPs solution. VSM magnetization cycles were measured by applying a field from -3000 to 3000 mT with a sampling rate of approximately 10 $mT.s^{-1}$.

II.6.12 MTT assay

First, 10 µL of MTT at 5 $mg.mL^{-1}$ was added to each well and the multi-well plate was then placed at 37 °C for 2 h of incubation. After medium removal, 100 µL of DMSO was added and a new incubation of 1 h at 37 °C was performed. The absorbance was then measured at 570 nm.

II.6.13 FITC-Annexin V / Propidium Iodide labelling

The cell death was analysed by Annexin V / Propidium Iodide (AnnV / PI) labelling 4 h after magnetic field exposure using a Cell Meter Annexin V apoptosis assay kit (AAT Bioquest, Sunnyvale, CA, USA) in accordance with the manufacturer's instructions. The counting of labeled cells was carried out through the analysis of confocal microscopy images (LSM510, Zeiss) representing populations of ~2,000 cells/experiment, using ImageJ software.

II.6.14 Statistical analysis on *in vitro* experiment results

Results are expressed as the mean ± SEM of at least three independent experiments. The statistical analysis was performed using One-way ANOVA test and Tukey post-hoc test. Differences were considered significant when $p < 0.05$ and the statistical significance was set as *$p < 0.05$, **$p < 0.01$, ***$p < 0.001$, ****$p < 0.0001$.

III Results and discussion

III.1 STMS growth on IO NPs through TEM imaging

View Article Online
DOI: 10.1039/D4NR01388C

III.1.1 Time-lapse TEM imaging

First, IO core NPs were synthesised by thermal decomposition and characterised as previously reported[47,48]. As it can be seen in **Figure S4**, the particles presented overall a spherical shape and a diameter of *ca*. 26.6±2.1 nm. The XRD pattern showed the characteristic diffraction peaks of the inverse spinel structure, with an additional peak that could come from residual NaCl salts from the synthesis (marked with *). These spinel IO NPs can be assimilated to oxidized magnetite ($Fe_{3-x}O_4$) as stated in several previous works achieved in our group[47,51,52]. Then, the IO NPs were used for the synthesis of IO@STMS NPs following the surfactant phase-driven sol-gel reaction shown in **Scheme 1** using an adapted and standardised protocol based on the one reported in previous works[44–46]. Briefly, the oleic-acid stabilised IO NPs stored in chloroform were suspended in dH_2O thanks to a phase transfer helped by the CTATos surfactant under high-speed stirring and at 65 °C. Controlled chloroform evaporation upon heating ensure phase transfer with establishments of hydrophobic interactions between surfactant molecules and the hydrophobic oleic acid bound to IO NPs. Apolar tails of surfactant and oleic acid interact by creating an interdigitated lipid-like bilayer. The positively charged external ammonium groups ensure electrostatic repulsion between the IO NPs in aqueous solution and overall a satisfying colloidal stability. Once the chloroform was evaporated and the CTATos-oleic acid stabilised IO NPs thus suspended in dH_2O, the TEOS precursor was added to the solution and condensed around the surfactant phase to form the STMS shell displaying large porosities.

The very first step of our study was to evaluate the possibility to control the STMS shell growth around the IO NPs core. To do so, we performed the “120 min” classical synthesis as described in the Materials and methods section (II.4) and collected a sample at different time points. The reaction in the sample aliquot was stopped by immersion in an ice bath and the particles were then washed prior to be imaged by TEM, as represented in **Scheme 2**. The obtained time-lapse of the reaction with the corresponding particle size distribution is presented in **Figure 1**. As it can be seen, few condensed silica spicules around the IO NPs can be observed at 5, 10, 20 and 30 min post-addition of TEOS, but a good silica layer with stellate morphology can be seen from 40 min. Its growth is then clearly observable at 50, 60, 90 and 120 min.

View Article Online
DOI: 10.1039/D4NR01388C

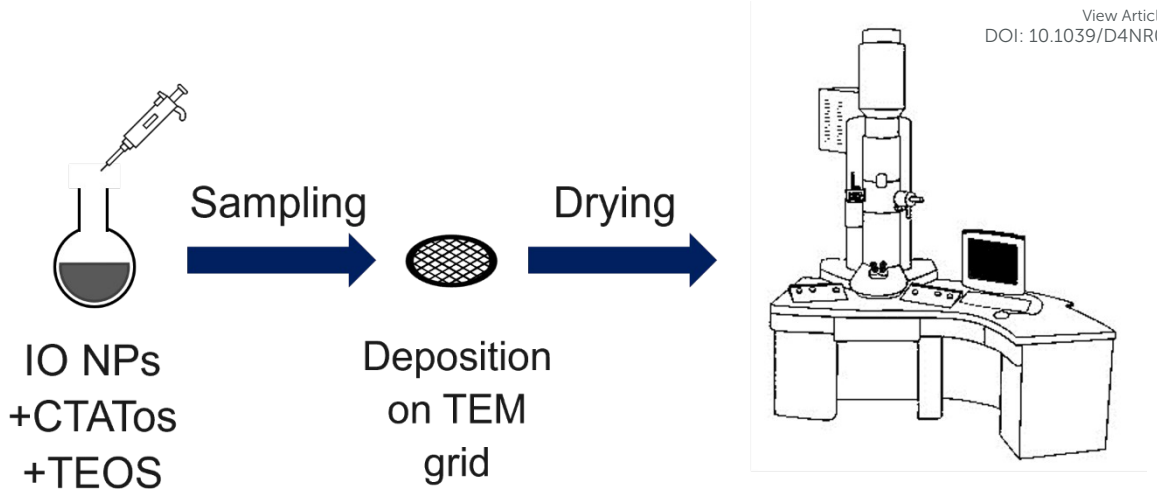

Scheme 2: Schematic representation of the procedure followed to perform time-lapse TEM imaging.

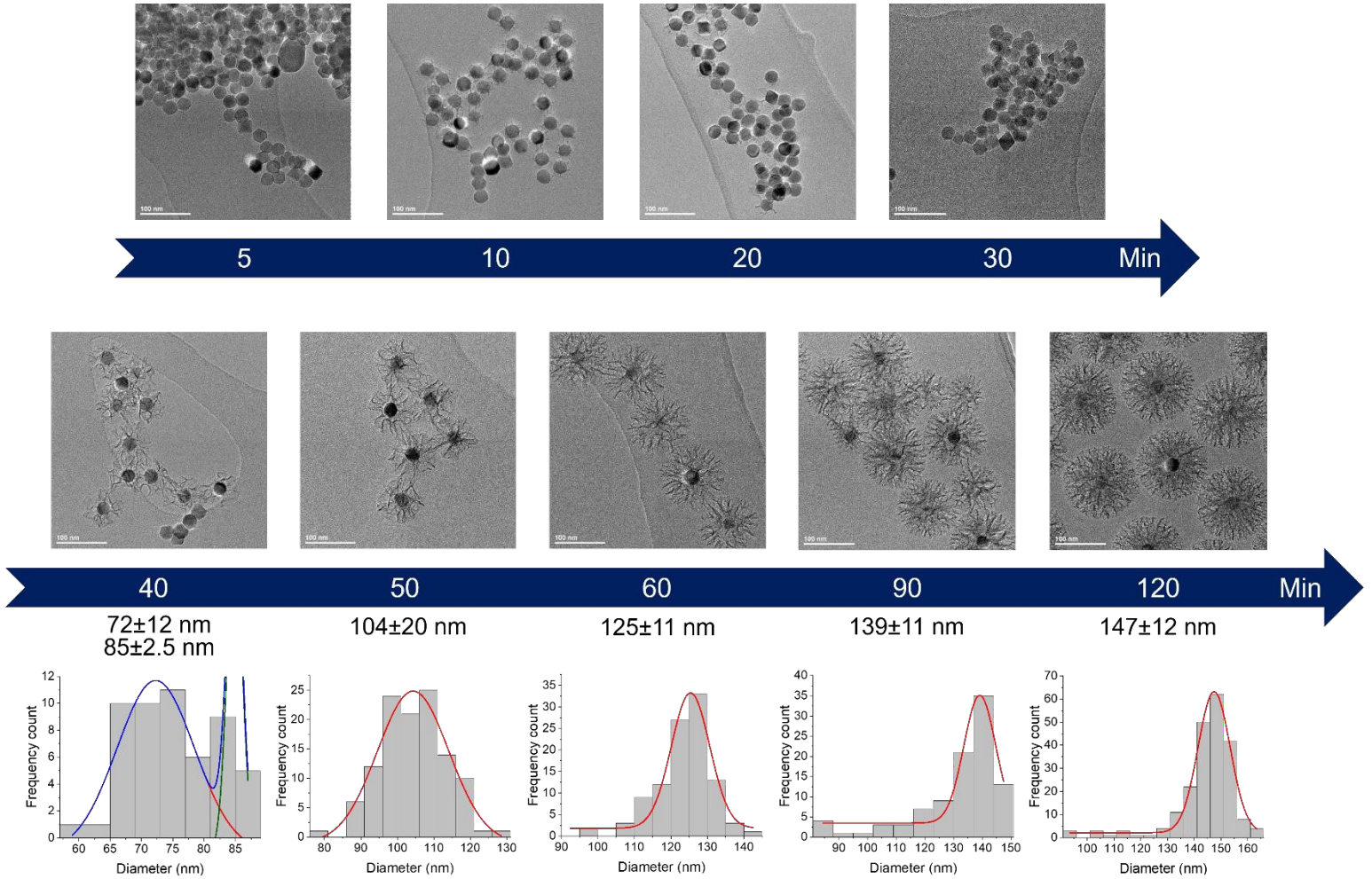

Figure 1: Kinetic tracking of the STMS growth on IO NPs by TEM with the corresponding IO@STMS NPs diameter distribution analysed by Gaussian fit.

View Article Online
DOI: 10.1039/D4NR01388C

EDX measurements were also performed on the samples (**Figure 2.A**) and shows a start of the silica growth between 20 min and 30 min post-addition of TEOS as the Si/Fe mass ratio increased from *ca*. 0.06±0.03 to *ca*. 0.13±0.03 and then to *ca*. 1.03±0.21 at 40 min post-addition of TEOS. Altogether, these analyses show that the STMS growth starts from 30 min post-addition of TEOS but that 40 min of reaction is necessary to get a good STMS shell. The reproducibility of this timing was evaluated on two other syntheses performed on different IO NPs batches. The evolution of the final IO@STMS NPs diameter determined by TEM is shown in **Figure 2.B** and confirms that the kinetics of the reaction remains the same from batch to batch.

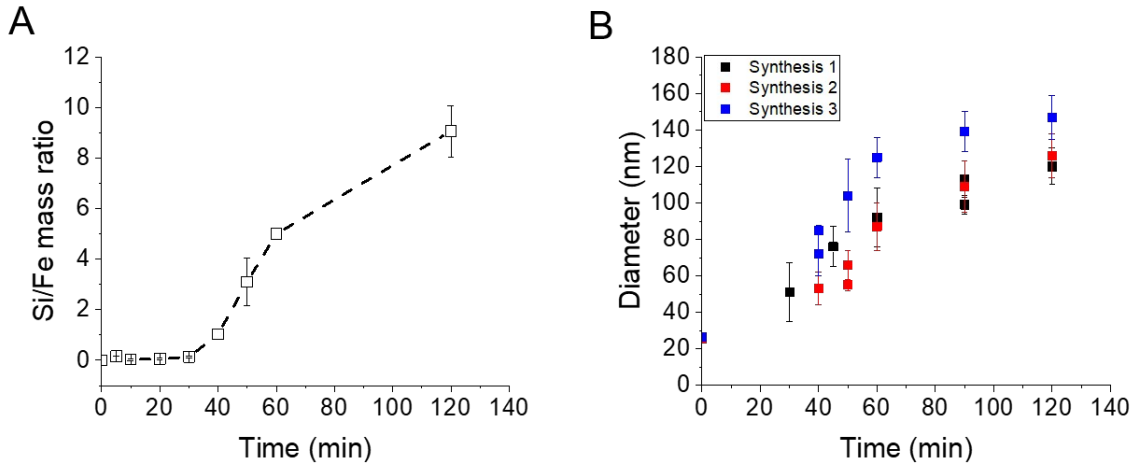

Figure 2: A) Kinetic tracking of the STMS growth on IO NPs by Si/Fe mass ratio obtained by EDX. B) Evolution of the IO@STMS NPs final diameter measured by TEM on three different syntheses.

All these experiments show that we can modulate the STMS shell thickness around IO NPs core by simply playing on the synthesis time and by taking into consideration that a minimum of 40 min of reaction is necessary to get a minimal STMS shell.

View Article Online
DOI: 10.1039/D4NR01388C

III.1.2 *In situ* LPTEM imaging

The development and application of sealed environmental cells TEM (EC-TEM) facilitates real-time monitoring of structural and chemical transformations in materials within reactive gas atmospheres at elevated temperatures, as well as (electro)-catalytic reactions in liquid environments. This innovative EC-TEM technology stands out as one of the most effective instruments for investigating local structure and material evolution in realistic environments, offering sub-nanometer resolution[53–55]. Given its capabilities, EC-TEM serves as the ideal tool for tracking the growth processes occurring at the STMS growth on the IO NPs. The procedure followed for the first attempt is represented in **Scheme 3**. Basically, it was chosen to prepare the IO NPs suspension in dH_2O, to place it in the chip, to find a region to observe by LPTEM and finally to inject the TEOS precursor. The obtained video is presented in **SI_Video1** and a time-lapse was extracted and is presented in **Figure 3**. It has to be noted that we worked in liquid phase, rendering the TEM focalisation harder than in dried phase. What can be specifically seen in these images is first the growing of a shadow around the IO NPs and then the growing of “arms” around the particles, particularly well seen in the last pictures. Such “arm” structure can also be seen on other particles that were imaged in another region of the chip (**Figure S5**). These arms are the silica shell growing around IO NPs and correspond quite well with the stellate structure of this shell.

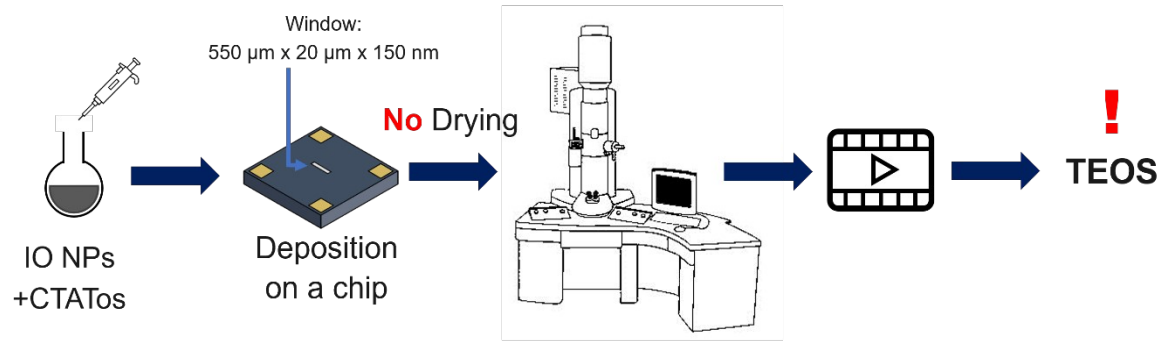

Scheme 3: Schematic representation of the procedure followed to perform the first *in situ* LPTEM experiment.

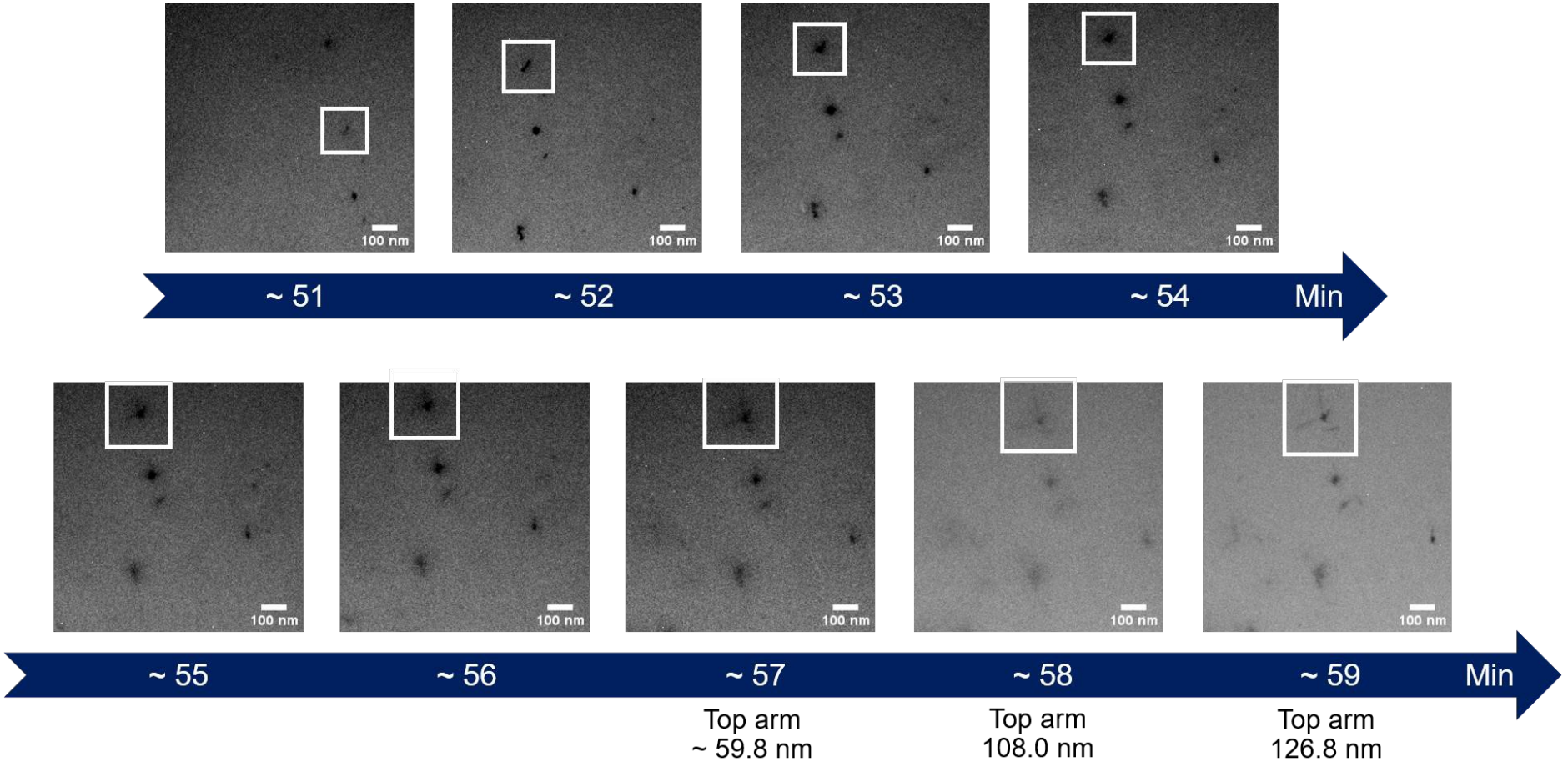

Figure 3: Time-lapse extracted from the *in situ* LPTEM video **SI_Video1**. The white box represents an interesting particle which diameter is measured on the last images.

View Article Online
DOI: 10.1039/D4NR01388C

The initial experiment provided an insightful glimpse into the silica growth on the IO NPs. However, we identified two key limitations: uncertainty regarding the timing of TEOS introduction into the cell, and concerns about the homogeneous dilution of TEOS on the cell. Thus, we performed a second experiment where we added the TEOS in the IO NPs suspension before adding the solution in the chip for *in situ* LPTEM observation, as represented in **Scheme 4**. The resulting video is given in **SI_Video2**, and the corresponding time-lapse is given in **Figure 4**. The growth of the STMS shell can clearly be seen by the increase of the size of most of the particles visible in the selected region. The diameter of one particle was measured all along the duration of the video, which here corresponds precisely to the time post-addition of TEOS. As evident from the extracted time-lapse (**Figure 4**) but also on the graph presented in **Figure 5**, the growth was quite fast between 50 and 60 min post-addition of TEOS, with a growing speed estimated at 8.1±0.5 $nm.min^{-1}$, but then it slowed down. This variation in growth kinetic compared to the experiment may stem from the confined conditions employed, without any stirring thus also under diffusion-limited conditions.

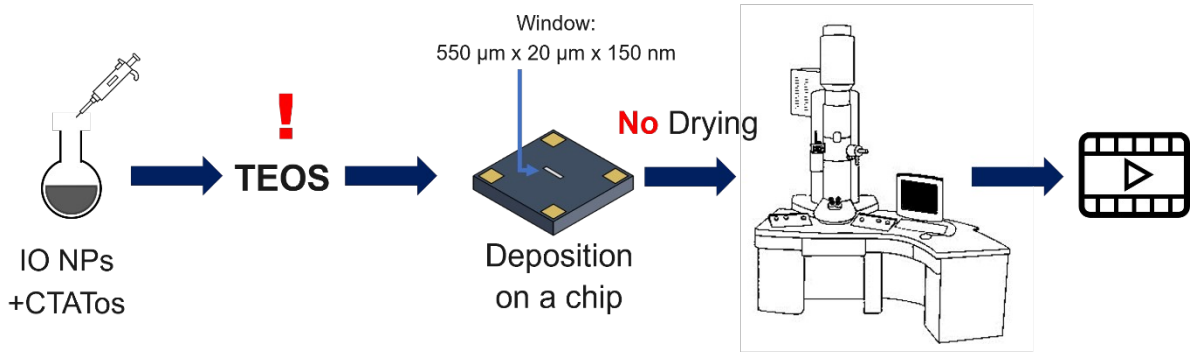

Scheme 4: Schematic representation of the procedure followed to perform the second *in situ* LPTEM experiment.

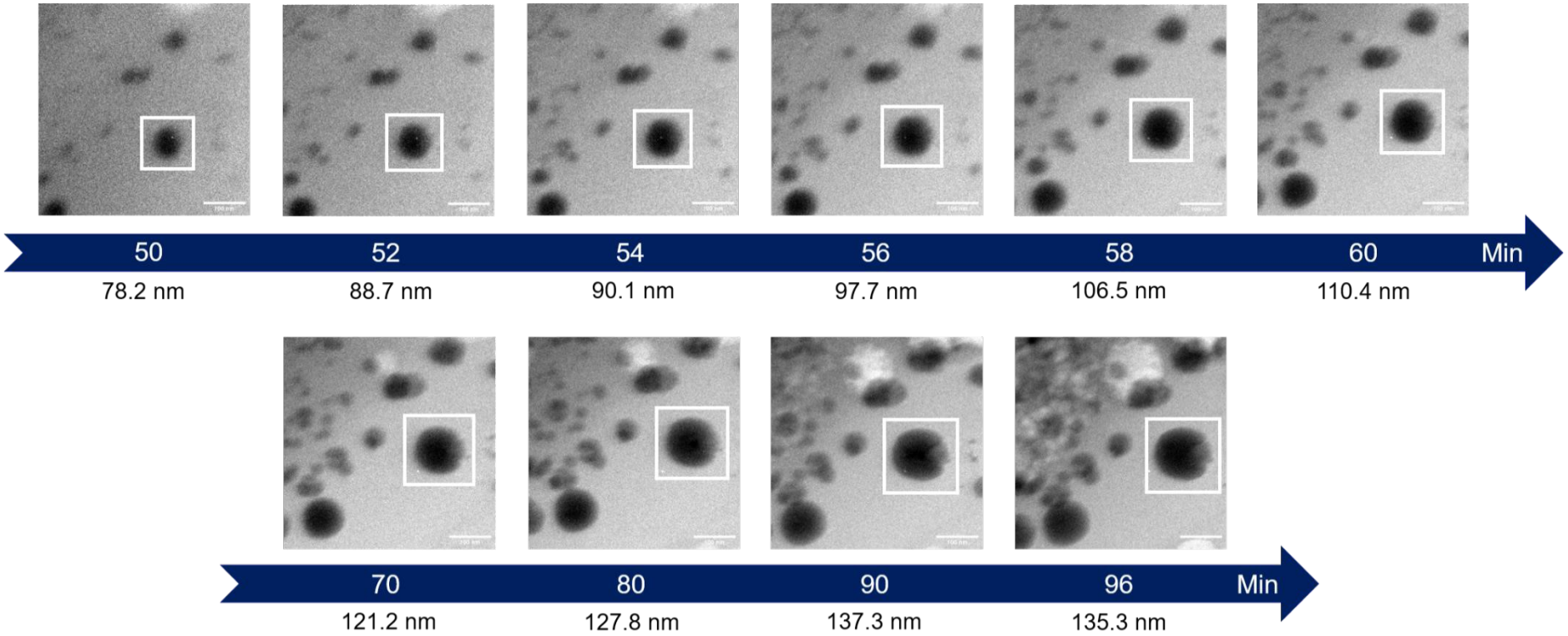

Figure 4: Time-lapse extracted from the *in situ* LPTEM video **SI_Video2**. The white box shows the particle which diameter is indicated under the images.

View Article Online
DOI: 10.1039/D4NR01388C

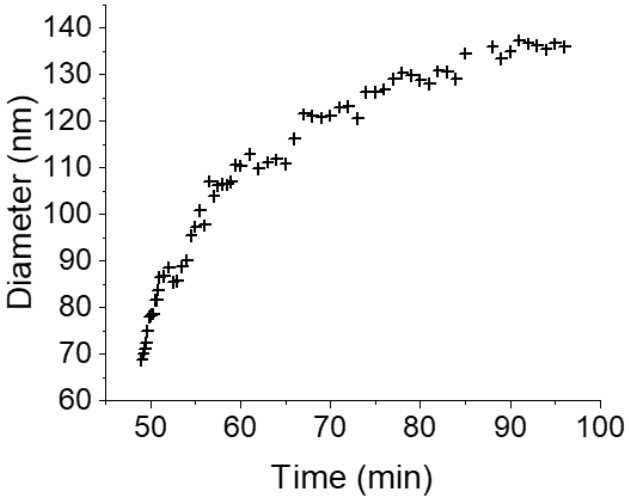

Figure 5: Evolution of the IO@STMS NPs final diameter measured on the *in situ* LPTEM images from **SI_Video2**.

These two attempts of *in situ* LPTEM imaging allowed us to obtain two complementary videos, one showing the “arm” structure of the stellate silica around the IO NPs, and the second showing the homogeneous growth of the silica shell on the IO NPs core.

III.2 Pore structure characterisation of tailored IO@STMS-t NPs

In a second step, we wanted to finely characterise the structural features of IO@STMS NPs having tuned shell thicknesses. For the sake of clarity, we denote the different batches IO@STMS-t where t represents the growth time for the rest of the study, and chose the times according to the previous results: 40, 60 and 120 min. Noteworthy that IO@STMS-t NPs usually come for the same IO NPs batch, but sometimes also from another IO NPs batch of very similar diameter. Such cases will be specified.

The **Figure 6** shows the synthesised particle batches from the first series (denoted series 1 for the rest of the study). The IO@STMS-120 were the ones obtained by performing the kinetic study. The IO@STMS-40 and IO@STMS-60 were synthesised in other experiments, whose respective diameters measured on TEM images correlates very well with the ones taken out during the kinetic study, as we got a

View Article Online
DOI: 10.1039/D4NR01388C

diameter here of *ca*. 87±18 nm versus *ca*. 85±2.5 nm during the kinetic study for 40 min of reaction and *ca*. 121±14 nm versus *ca*. 125±11 nm for 60 min, showing again the good reproducibility of the synthesis and feasibility of the control of the STMS shell thickness.

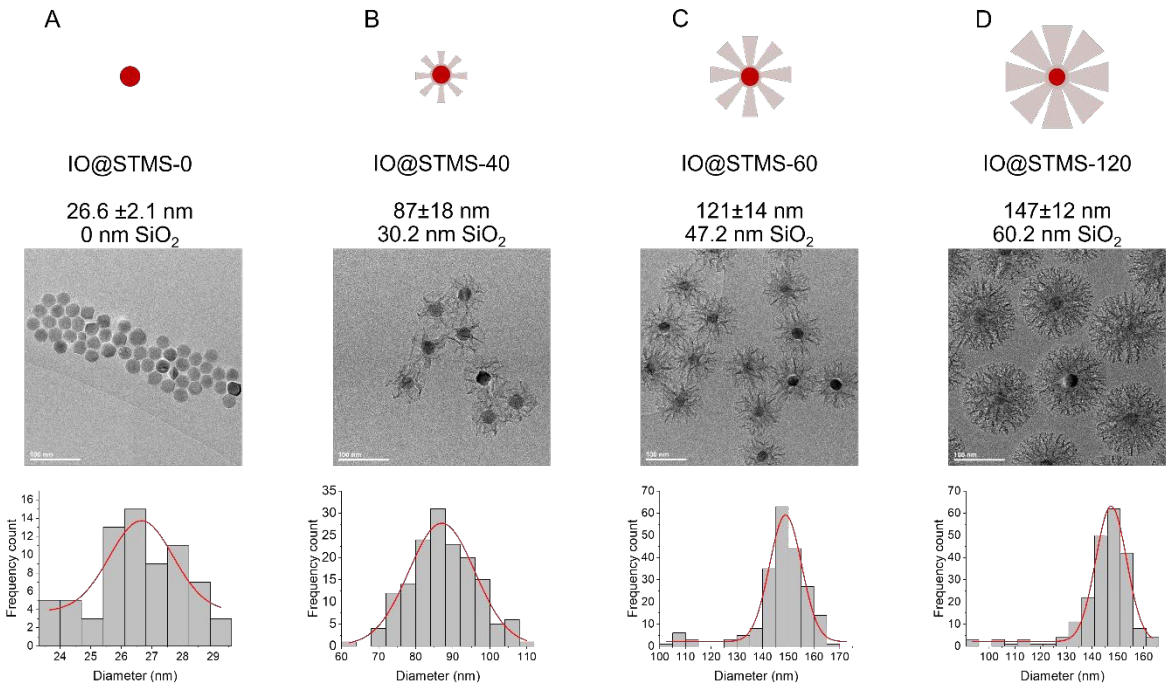

Figure 6: Schematic representation, TEM and distribution of diameters for A) IO@STMS-0, B) IO@STMS-40, C) IO@STMS-60 and D) IO@STMS-120 obtained from series 1.

We then characterised the porous texture/structure of the IO@STMS-t by nitrogen adsorption-desorption measurements in order to get precise information on the structural characteristics of the particles in terms of surface area, pore size, and pore volume (**Figure 7**). We also added IO@STMS-90 to this porous texture study as it gave the same diameter than the IO@STMS-120 (*ca.* 149±12 nm, see **Figure S6** for the TEM characterisation). In addition, for this characterisation, we had to synthesise a new batch of IO@STMS-40 due to very low quantity obtained for the batch presented in **Figure 6** (see **Figure S7** for the TEM characterisation).

The nitrogen adsorption-desorption curves are presented in **Figure 7** and the BET surface (S_{BET}), pore volume (V) and representative pore size (D_p-) values are regrouped in **Table 1**. Firstly, the global aspect of adsorption-desorption isotherms

View Article Online
DOI: 10.1039/D4NR01388C

(**Figure 7.B, E, H, K**) shows the dual micro-mesoporous character of our samples. Indeed, the shape of the curve at relative pressure up to 0.6, with the small increase and then the plateau, corresponds more to a type I isotherm (according to the IUPAC classification) which is attributed to microporous materials (pore size below 2 nm); while the presence of the sharp increase at higher relative pressure (from 0.8) with the small hysteresis loop corresponds more to a type IV or V isotherm, which is attributed to mesoporous materials (pore size from 2 to 50 nm)[56]. Unfortunately, the non-representative shape of the hysteresis loop does not allow the determination of the pore shape. However, other characteristics could be extracted from the nitrogen adsorption-desorption measurements.

View Article Online
DOI: 10.1039/D4NR01388C

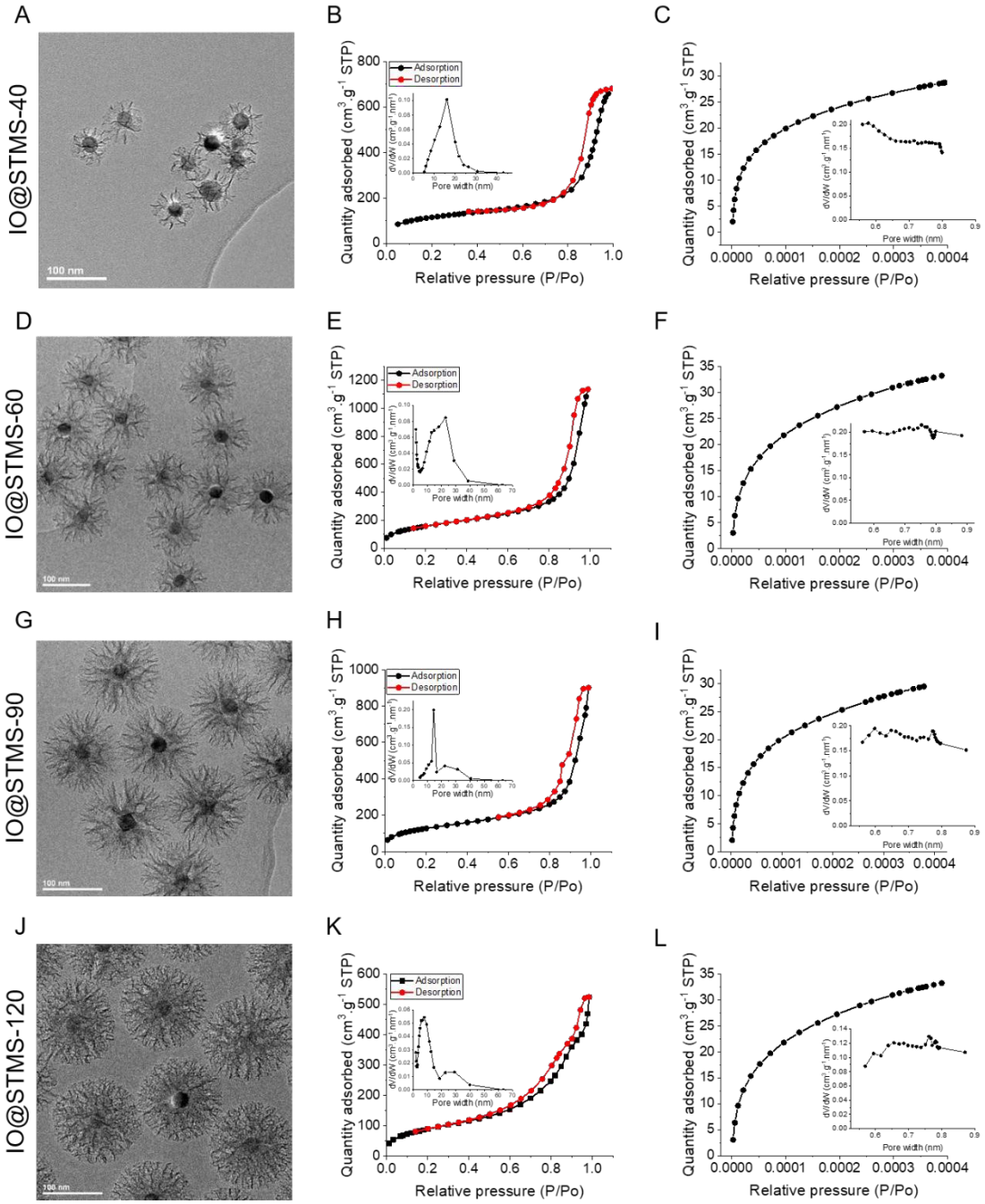

Figure 7: TEM images (issued from Fig. 6, Fig S6 and S7), adsorption-desorption isotherms at high relative pressure including an inset with the BJH desorption pore volume plot and adsorption isotherm at small relative pressures including an inset with the Horvarth-Kawazoe differential pore volume plot for IO@STMS-40 (A, B, C), IO@STMS-60 (D, E, F), IO@STMS-90 (G, H, I) and IO@STMS-120 (J, K, L).

View Article Online
DOI: 10.1039/D4NR01388C

Table 1: Textural properties of the IO@STMS-t NPs (t>0).

Sample	S_{BET} ($m^2.g^{-1}$)	V_{pores} ($cm^3.g^{-1}$)	V_{meso} ($cm^3.g^{-1}$)	V_{micro} ($cm^3.g^{-1}$)	$D_{p\text{-}micro}$ (nm)	$D_{p\text{-}meso}$ (nm)
IO@STMS-40	408	1.03	0.92 (a)	0.041	0.5-0.8	16.1
IO@STMS-60	579	1.59	0.99 (b)	0.063	0.5-0.8	15.2
IO@STMS-90	466	1.16	0.70 (c)	0.056	0.5-0.8	14.5
IO@STMS-120	333	0.67	0.52 (c)	0.034	0.5-0.8	7.7

V_{meso} was determined by integrating the BJH pore volume plot between 5 and 24 nm (a) or between 5 and 18 nm (c). In the specific case of IO@STMS-60, the signal was decomposed to get the participation of the mesopores and the voids and the integration was performed according to the obtained peaks, thus from 5 to 39 nm (b). V_{micro} was determined by integrating the Horvarth-Kawazoe differential pore volume plot between 0.5 and 0.8 nm.

Secondly, the BET surface area could be determined and it is clear that the value decreases as the silica growth time increases, as it dropped from *ca.* 579 $m^2.g^{-1}$ for IO@STMS-60 to *ca.* 466 $m^2.g^{-1}$ and *ca*. 333 $m^2.g^{-1}$ for IO@STMS-90 and IO@STMS-120 respectively. The global pore volume followed the same trends, as it dropped from *ca*. 1.59 $cm^3.g^{-1}$ for IO@STMS-40 to *ca*. 1.16 $cm^3.g^{-1}$ and *ca*. 0.67 $cm^3.g^{-1}$ for IO@STMS-90 and IO@STMS-120 respectively. These first observations mean that increasing the reaction time allows the STMS shell first to grow rapidly in a radial way (from the NPs to the exterior), thus getting a higher silica shell thickness with large openings and thin walls, and then to condensate inside the pores, thus getting a denser shell and thicker walls. One can object that the BET values and the global pore volume measured for the IO@STMS-40 are smaller (*ca*. 408 $m^2.g^{-1}$ and *ca*. 1.03 $cm^3.g^{-1}$ respectively) than the ones of IO@STMS-60 and thus do not follow the trend, but this is actually logical as the particles are still very small, especially for the batch used for this measurement. However, this kind of mechanism of the STMS shell growth, that we represented in **Scheme 5**, is in great correlation with what is observed by TEM: we can clearly see large pores in the TEM picture “40 min” that we do not longer see in the TEM picture “120 min” in **Figure 1**, and the thin wall reminds the silica “arms” seen in the first *in situ* LPTEM experiment (**Figure 3** and **Figure S5**). In addition, the comparison of the IO@STMS-90 and IO@STMS-120 leads to the conclusion that even if the radial growth is done, the condensation reaction still occurs, reducing the global pore volume and resulting in a denser silica shell.

View Article Online
DOI: 10.1039/D4NR01388C

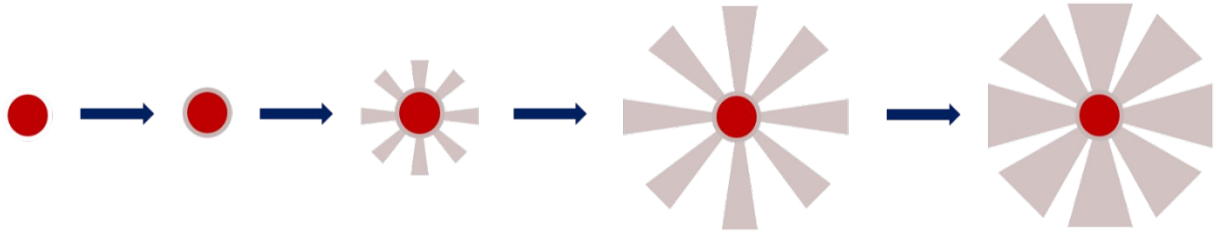

Scheme 5: Schematic representation of the STMS shell growth mechanism around IO NPs core.

We nevertheless note that this global pore volume includes the volume of the micropores (V_{micro}), the volume of the mesopores (V_{meso}) and the void volume corresponding to interparticle spaces. We thus used the Horvarth-Kawazoe model (inset in **Figure 7.C, F, I, L**) and the BJH model (inset in **Figure 7.B**, **E, H, K**) to extract the V_{micro} and V_{meso} and respectively their associated representative pore width. The values reported in **Table 1** confirms that we have a micro-mesoporous structure as the V_{meso} does not corresponds to the total V_{pore}. The high values of V_{meso} compared to V_{micro} were expected as, even if the micropores are present in a large amount as ultra-thin channels (around 0.5-0.8 nm diameter), they do not contribute importantly in the total pore volume and the mesopores still represent a largely higher volume. Furthermore, the Horvarth-Kawazoe differential pore volume plot does not allow determining a representative micropore size. However, the decrease of the V_{micro} with the increase of the growth time is clear, and the quite low value of the V_{micro} for IO@STMS-120 (*ca*. 0.034 $cm^3.g^{-1}$) tends to show that the microporous component of the sample has been highly reduced by the silica condensation. The decrease of the V_{meso} with silica growth time also seems logical given the previous conclusions. Regarding the pore size analysis, the evolution of the BJH desorption pore volume plot is quite interesting. Indeed, the plots show a bimodal distribution for IO@STMS-90 and IO@STMS-120, corresponding to a $D_{p\text{-}meso}$ of *ca.* 14.5 nm and *ca*. 7.7 nm respectively with another small peak around 30 nm that is usually attributed to interparticles voids. However, the plot obtained for IO@STMS-40 and IO@STMS-60 do not show a bimodal distribution, meaning that the mesopores are still quite “open” up to 60 min of synthesis, *i.e*. large enough not to be very different of interparticle

View Article Online
DOI: 10.1039/D4NR01388C

voids on the plot. However, the analysis of these plots allowed determining a $D_{p\text{-meso}}$ of
ca. 16.1 nm and *ca*. 15.2 nm for IO@STMS-40 and IO@STMS-60 respectively, which follows the global trends found with IO@STMS-90 and IO@STMS-120.

Altogether, these analyses confirm the micro-mesoporous character of the IO@STMS-t NPs and showed that the radial growth of the STMS shell is accompanied by a continuous silica condensation of the shell, even when the radial growth is stopped.

III.3 Colloidal stability of tailored IO@STMS-t NPs

Finally, the influence of the reaction time and thus of the STMS shell thickness on the colloidal stability of the particles was evaluated in EtOH (**Figure S8**) and in dH_2O (**Figure 8**). The stability of the IO-CTA+ NPs in dH_2O (IO@STMS-0) was quite good after the phase transfer from chloroform to CTATos solution in dH_2O. The hydrodynamic diameter was determined to be *ca.* 45.9±15.9 nm which indicates that some aggregates may be formed even with the surfactant covering. This is in correlation with the aggregation of the particles that we observed after a 24 h aging. Regarding the IO@STMS-t (with t>0) NPs, the colloidal stability was overall good in both EtOH and dH_2O. The size graphs in intensity distribution show some very slight aggregate with the smaller STMS shell thickness and a progressive disappearance of these aggregates with the increase of the STMS shell thickness in both solvents. In addition, the size graphs in number distribution show that these aggregates were very few in the sample as only one peak is visible. Interestingly, the hydrodynamic diameter was measured to be *ca*. 198±2.4 nm (PDI *ca*. 0.24±0.01), *ca*. 174±0.3 nm (PDI
ca. 0.19±0.02) and *ca*. 177±0.9 nm (PDI *ca*. 0.07±0.01) in EtOH and *ca*. 183±2.4 nm (PDI *ca*. 0.27±0.02), *ca*. 163±0.8 nm (PDI *ca*. 0.18±0.02) and *ca*. 171±1.1 nm (PDI *ca*. 0.07±0.02) in dH_2O for IO@STMS-40, IO@STMS-60 and IO@STMS-120 respectively, indicating suitable colloidal stability.

View Article Online
DOI: 10.1039/D4NR01388C

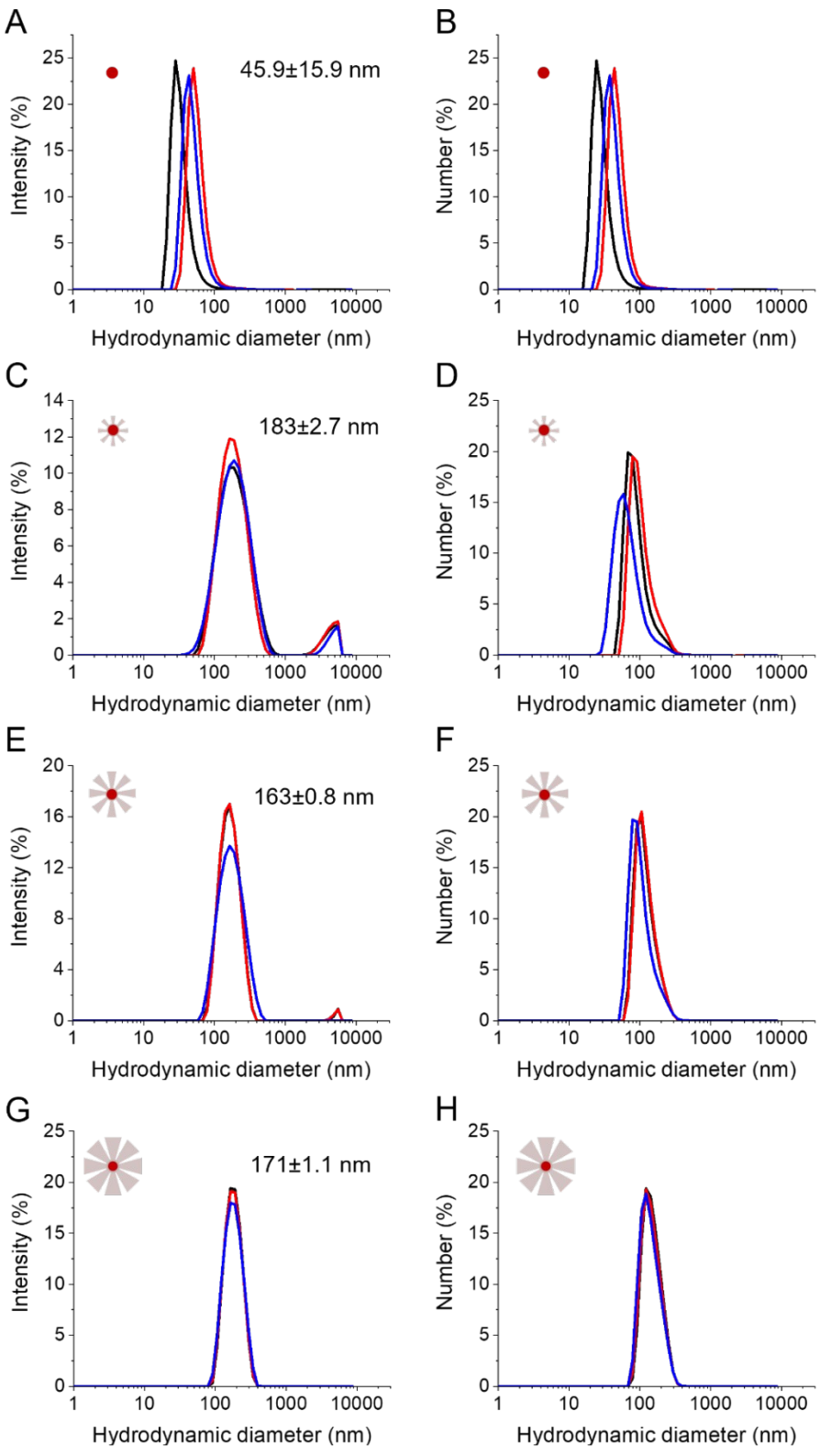

Figure 8: Colloidal stability in dH_2O as shown from the distributions in intensity and in number of hydrodynamic diameters respectively of IO@STMS-0 (A, B), IO@STMS-40 (C, D), IO@STMS-60 (E, F) and IO@STMS-120 (G, H).

View Article Online
DOI: 10.1039/D4NR01388C

The zeta potential of the particles was evaluated in dH_2O right after the colloidal stability study (**Figure S9**). The change from positive value (*ca.* 45.4±0.6 mV) for IO@STMS-0 to negative value for IO@STMS-t (*ca*. -23.5±0.2 mV, *ca*. -21.6±0.2 mV and *ca*. -14.8±0.8 mV for t=40, 60 and 120 respectively) is due to the silica shell around the particles and was used, in practice, as a first indicator of the success of the silica synthesis before any TEM analysis. Given the colloidal stability, and more precisely the disappearance of the slight aggregates when the growth time increases, we were expecting an increase in absolute value of the zeta potential with the increase of the growth time, as a higher absolute value would mean a higher electrostatic repulsion and thus a higher stability. However, the trend follows the other evolution, and this may be explained by the nature of the negative surface charge in silica NPs. Indeed, this negative surface charge comes from the silanolate groups, that are coming from easily deprotonated Si-OH groups at the NPs surface. When the growth time increases, the surface area decreases and Si-OH may cross-link more into Si-O-Si bridge groups, both effects contributing to reduce the negative zeta value.

Further, we found that IO@STMS with small STMS shell thickness have similar/comparable hydrodynamic size that IO@STMS with bigger shell (in the range 163-183 nm). We figure out that clusters composed of a couple to several NPs are formed for IO@STMS-40 (TEM core shell size of *ca*. 87±18 nm) while the IO@STMS-120 may be dispersed individually. Factors such as the increase of the hydrophilicity of the silica coating combined with the absence/reduction of magnetic dipolar interactions between iron oxide cores may explain this enhanced dispersion state for bigger shells. Conversely, incomplete growth of silica that may favour H-bonds interactions between surface silanol groups of small STMS shell combined with potential magnetic dipolar interactions would explain their stabilisation into small clusters of several IO@STMS NPs. For instance, the difference of dipolar magnetic interactions existing between citrate stabilised iron oxide NPs and silica coated iron oxide was well evidenced by Kesse, Vichery and coworkers using ZFC/FC curves[57].

Overall, the DLS analyses show that the increase of the STMS shell thickness improves the global colloidal stability of the IO@STMS-t NPs.

View Article Online
DOI: 10.1039/D4NR01388C

III.4 Influence of the STMS shell on MRI, MHT and PHT properties of IO NPs

We showed in the previous sections that we were able to synthesise IO@STMS NPs with tunable silica shell thicknesses and pore structures. The next step of our study was to investigate the influence of the STMS shell thickness on the MRI, MHT and PHT properties of the IO NPs core. From this section, it was particularly important for us to compare IO@STMS-t NPs with the same IO NPs core, thus coming from the same series of synthesis. The series 1 presented in **Figure 6** allowed only one measurement for the following experiments. We thus synthesised a second series of IO@STMS-t NPs (denoted as series 2) which characteristics are given in **Figure S10**, for which we could perform the measurements in triplicate and the *in vitro* studies with cancer cells presented in the last section of this article.

III.4.1 Magnetic Resonance Imaging (MRI)

MRI is based on the nuclear magnetic resonance of the hydrogen atoms of water molecule (or other tissues) under a static magnetic field (typically 1.5 T) and after stimulation with a radiofrequency field. Protons relax with time through two modes of relaxation and contrast agents such as magnetic core-shell NPs influence strongly these relaxation times with their concentration. These relaxation times are the longitudinal relaxation denoted T_1 and the transverse relaxation denoted T_2, and their measurement give access to the respective longitudinal and transverse relaxivities r_1 and r_2 that characterise contrast agents. Thus, we measured the longitudinal and transverse relaxation rates ($R_1=1/T_1$ and $R_2=1/T_2$ respectively) at different iron concentrations (**Figure 9.A** and **9.B**) for the different IO@STMS-t NPs. As it can be seen in **Figure 9.C**, the longitudinal relaxivity r_1 is not impacted by the presence of a short STMS shell, as it decreased only from *ca.* 8.7±0.2 $mM^{-1}.s^{-1}$ for IO@STMS-0 to *ca.* 8.1±1.3 $mM^{-1}.s^{-1}$ for IO@STMS-40 (STMS shell thickness of *ca*. 20.8 nm). However, this value decreased importantly when increasing the STMS shell thickness as it dropped to *ca.* 2.6±0.1 $mM^{-1}.s^{-1}$ and *ca.* 1.2±0.1 $mM^{-1}.s^{-1}$ for IO@STMS-60 and IO@STMS-120 respectively, which corresponds to a STMS shell thickness of *ca.* 30.8 nm and *ca.* 42.3 nm respectively. This tendency was also followed by the IO@STMS-t NPs obtained in the series 1, as it can be seen in **Figure S11.C** and **Table S1**. This phenomenon can be explained by the fact that the longitudinal relaxation is based on an intern sphere mechanism where the proton

View Article Online
DOI: 10.1039/D4NR01388C

relaxation occurs through a direct contact probably through iron-OH_2 (metal-ligand bond) with the contrast agent. So, in our case, it is highly dependent of the access of water to the IO core NP. Thus, the increase of the STMS shell thickness, together with the linked decrease of the pore volume associated to silica shell densification, decreases this access to water and then the r_1 value.

Regarding the transverse relaxivity r_2 (**Figure 9.D**), the value is slightly increased in the presence of the STMS shell, with a very slight increase of the r_2 value when the shell thickness increases. Indeed, the r_2 went from *ca.* 356±17 $mM^{-1}.s^{-1}$ for IO@STMS-0 to *ca.* 345±9 $mM^{-1}.s^{-1}$, *ca.* 380±5 $mM^{-1}.s^{-1}$ and *ca.* 409±6 $mM^{-1}.s^{-1}$ for IO@STMS-40, IO@STMS-60 and IO@STMS-120 respectively. The IO@STMS-t NPs obtained from series 1 gave the same tendency as shown in **Figure S11.D** and **Table S1**. The first observation that can be drawn here is that the silica shell growth does not influence or hinder importantly these transverse relaxation modes of water protons. This is attributed to the long-range effect of this relaxation mode through dipolar interactions due to the high magnetic moment of the IO NPs. We can notice the slight r_2 increases from 0 to t min growth time which may be due to the colloidal stabilization brought by the STMS shell to the IO NPs and increase of the hydrodynamic diameter, slowing down their Brownian motion and increasing the contact time between the water molecules and the IO NPs during the spin echoes. Importantly, the r_2 values are very high compared to commercial T_2 contrast agents (Combidex r_2 = 65 $mM^{-1}.s^{-1}$, Ferumoxytol r_2 = 89 $mM^{-1}.s^{-1}$, Resovist r_2 = 189 $mM^{-1}.s^{-1}$)[58] showing that these IO@STMS-t NPs are very good T_2 contrast agents[46,59,60].

View Article Online
DOI: 10.1039/D4NR01388C

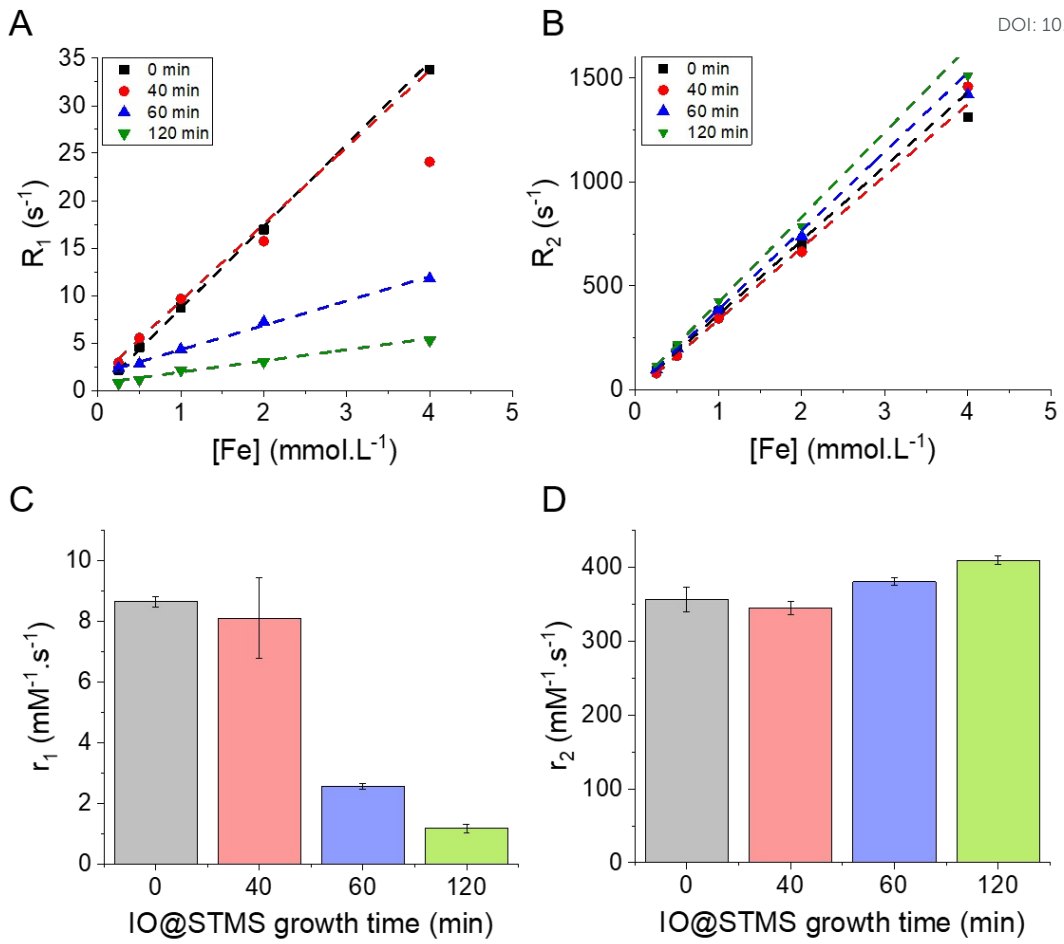

Figure 9: A) and B) respectively the longitudinal $R_1=1/T_1$ (s^{-1}) and transverse $R_2=1/T_2$ (s^{-1}) relaxation rates as a function of the concentration in iron in the different IO@STMS-t NPs solutions. C) and D) respectively the evolution of the longitudinal and transverse relaxivities r_1 and r_2 as a function of the IO@STMS growth time. These results were obtained with the IO@STMS-t obtained from series 2.

III.4.2 Magnetic Hyperthermia (MHT)

As long as the frequency and amplitude respect the so-called Brezovich criterion[50], the application of AMF is non-invasive, non-toxic and does not have a tissue penetration depth limit. More importantly, magnetic hyperthermia (MHT) allows the local increase of body temperature from 37 °C to 40-43 °C, which is enough to kill cancer cells as they are more sensitive to temperature than healthy cells[3]. This ability to induce MHT is already used in preclinical and clinical trials[7–9], with the notably trial conducted in Berlin (Germany) by MagForce with NanoTherm™ technology where

View Article Online
DOI: 10.1039/D4NR01388C

cancer cell apoptosis was shown to be induced by MHT. The use of IO NPs as bimodal agents for MRI and MHT has also been studied and reported[44,46,61].

The release of heat from IO NPs under AMF stimulation is usually described as arising from two phenomena: the Néel relaxation, which corresponds to the reorientation of the magnetic moment inside the particle, and the Brown relaxation, which corresponds to the reorientation of the whole particle in the medium. The heating process depends on several parameters such as the magnetocrystalline anisotropy, the NPs volume and the environment viscosity. Usually, the heating capacity of particles is expressed with the Specific Absorption Rate (SAR), which is most often determined by a calorimetric experiment through **Eq. 3**, given in the Materials and methods (II.6.10). Another way to determine the SAR consists in measuring the dynamic magnetization M(t), which exhibits a phase shift compared to the instantaneous AMF vector H(t), creating AC hysteresis loops, even for superparamagnetic IO NPs. In this AC magnetization curve $M_t(H_t)$, the surface area is equal to the heat dissipated during one period of the AMF $T=2\pi/f$, hence the SAR[50]:

$$SAR\ (\mathrm{W{\cdot}g^{-1}}) = \frac{\mu_0}{m_{\mathrm{IO}}} \times f \times \oint_{\mathrm{cycle}}^{T} M_t(H_t)\, dH_t \quad (Eq.\ 2)$$

where μ_0 is the magnetic permeability of vacuum and m_{IO} is the mass of iron oxide in g (obtained as $m_{IO}=1.38 \times m_{Fe}$).

The magnetothermal properties of the particles obtained from series 2 were evaluated by AC magnetometry using different conditions of frequency/magnetic fields f/H: 280 kHz/20kA.m^{-1}, 280 kHz/24 kA.m^{-1} and 217 kHz/24 kA.m^{-1} for IO@STMS-0 (3.35 mgFe.mL^{-1}) and for IO@STMS-t, with t=40,60,120 min (0.5 mgFe.mL^{-1}). Representative hysteresis cycles are presented in **Figure 10.A-C**, where it can be noted that the ones obtained for IO@STMS-0 present a "square shape" rather than opened sigmoids. In previous work by Mille *et al*.[62], this phenomenon of large opening of the hysteresis loops was ascribed to the organisation of the particles as chains of NPs during the magnetic field application. The chaining effect was also investigated by Martinez-Boubeta, Serantes and coworkers[63,64]. The authors showed experimentally and using modelling that the formation of chain-like structures was explained by more favourable dipolar

View Article Online
DOI: 10.1039/D4NR01388C

interactions energy as compared to the thermal energy. Computation of hysteresis cycles evolution was achieved as a function of the number of particles within a chain and indicated that hysteresis cycles had more squared shapes and that the area of hysteresis loop increased (and thus SAR values) with the length of the chain.

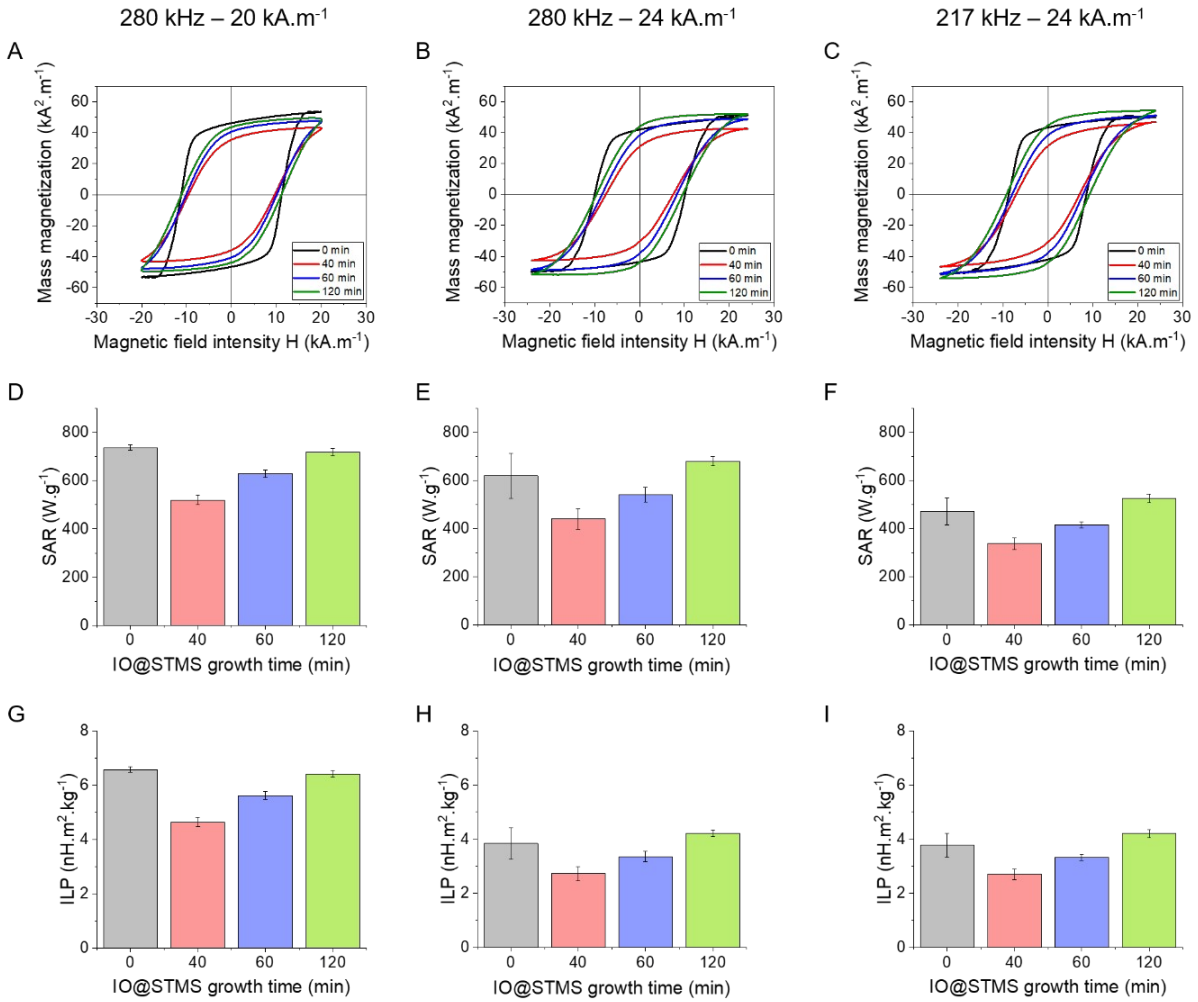

Figure 10: A), B) and C) Representative hysteresis cycles for the different IO@STMS-t NPs (IO@STMS-0 and for IO@STMS-t (t=40,60,120 min)) obtained from series 2 at different frequency-amplitude conditions. D), E) and F) Corresponding SAR values. G), H) and I). Corresponding ILP values.

In our case, macroscopic chains were indeed observed after the AC magnetometry measurement, which could be redispersed by sonication after the measurement. Such chains were also observed on some regions when performing the *in situ* LPTEM imaging (**Figure S12**)**.** This chaining is likely explained by the large

View Article Online
DOI: 10.1039/D4NR01388C

diameter of the IO NPs cores (d_{core}=26.6 nm), which given the measured saturation magnetization of these $Fe_{3-x}O_4$ NPs achieved in **Figure S13** (56.5 emu.g^{-1} hence M_S=2.83×10^5 A.m^{-1} volume magnetization) leads to a dipolar parameter $\gamma = \frac{\mu_0 M_S^2 \pi^2 d_{core}^3}{36 k_B T} \sim 125$, which explains why the bare IO NPs (without silica) make chains. When the silica layer grows, the dipolar parameter decreases to much lower values $\gamma = \frac{\mu_0 M_S^2 \pi^2 d_{core}^6}{36 k_B T \cdot (d_{core}+2\delta_{shell})^3} \sim 5.0$ for IO@STMS-40 (δ_{shell}=30.2 nm), ~ 2.1 for IO@STMS-60 (δ_{shell}=47.2 nm) and, ~ 1.4 for IO@STMS-120 (δ_{shell}=60.2 nm).

Regarding evolution of the saturation magnetizations Ms (referred to iron oxide mass) as a function of the silica shell growth presented in **Figure S13**, it is worthy to note that Ms tends to decrease when the silica shell is reduced. Ms of these samples were measured several months after their synthesis and we hypothesize that when large silica shell is formed, the oxidized magnetite ($Fe_{3-x}O4$) is preserved from oxidation with time while by decreasing silica shell, oxidation in maghemite (γ-Fe_2O_3) is favoured, explaining this lowering of Ms.

Looking at the SAR values, presented in **Figure 10.D** (280 kHz and 20 kA.m^{-1}) the presence of the STMS shell on the IO NPs core tends first to decrease the SAR, as it dropped from *ca.* 736±11 W.g^{-1} for IO@STMS-0 to *ca.* 520±20 W.g^{-1} for IO@STMS-40. The SAR values then increased with the increase of the STMS time growth as it was measured at a value of *ca.* 629±16 W.g^{-1} and *ca.* 718±15 W.g^{-1} for IO@STMS-60 and IO@STMS-120 respectively under the same magnetic field. The same tendency is visible for the two other magnetic fields (**Figure 10.E** and **F**) and the global tendency could also be found for the particles obtained in series 1, which results are presented in **Figure S14** and **Table S2**. The global reduction of the SAR with the addition of the silica shell is in agreement with previous studies performed in our team[65] and could correspond to the disappearance of the observed magnetic chains of iron oxide@CTA+ (IO@STMS-0) when silica coating is achieved. With a small silica shell, the core shell reorganised in small clusters which might have a limited Brownian relaxation. Then, the increase of the SAR with the increase of the silica shell could come from the better colloidal stability brought by this higher shell thickness, which restores the Brown relaxation mechanism to the heat dissipation.

Unfortunately, the SAR values are difficult to compare from one article to another as it is very dependent of extrinsic parameters such as the frequency f and the amplitude H of the applied magnetic field[66]. Thus, we calculated the Intrinsic Loss

View Article Online
DOI: 10.1039/D4NR01388C

Power (ILP) following the **Eq. 4** given in the Materials and methods (II.6.10), which assumes a linear dependency of SAR with f and quadratic with H, as predicted by the linear response theory for superparamagnetic NPs[67].

Such calculations gave us an ILP ranging from *ca*. 4.64±0.18 to *ca*. 6.58±0.10 $nH.m^2.kg^{-1}$ for the series 2 at 280 kHz and 20 $kA.m^{-1}$ (**Figure 10.G**) and then from *ca*. 2.7±0.27 to 4.21±0.12 to $nH.m^2.kg^{-1}$ when the amplitude is increased to 24 $kA.m^{-1}$ (**Figure 10.H** and **I**). The moderate decrease of the SAR and ILPs values at 24 $kA.m^{-1}$ can come from the fact that the measurements were performed on the same samples and some days after the ones performed at 20 $kA.m^{-1}$. We suppose here that the chaining effect happened in the first place and was beneficial for the SAR and thus the ILP, while the aging of the samples led to aggregates that could not be completely broken with the sonication and thus reduced the ILPs. What can be noted is that these reduced values correlate well with the one obtained for series 1 (from *ca*. 2.11 $nH.m^2.kg^{-1}$ (IO@STMS-40) to *ca*. 4.08 $nH.m^2.kg^{-1}$ (IO@STMS-0) (**Figure S14.C** and **Table S2**)). In addition, such values are quite good compared to the ILP of 1.18 $nH.m^2.kg^{-1}$ measured for NanoTherm™ [68] and compared to the ILPs reported in the literature[10], which is very encouraging for anti-cancer application using MHT therapies.

III.4.3 NIR-light photo-induced Hyperthermia (PHT)

Even if NIR light irradiation suffers from a tissue penetration of only 3-4 cm[69,70], this technique can be simply implemented and at low cost. The potential of IO NPs as heating agents under such stimulus has recently emerged with a first publication using them to induce photonic hyperthermia (PHT) from Yu *et al*. in 2011[14]. The dual use of MHT and PHT is also studied. For example, Espinosa *et al.* reported that the hyperthermia induced by the administration of both stimuli to cubic IO NPs led to the complete tumour regression in an *in vivo* model, explaining that the use of PHT restores the MHT efficiency after cell internalisation, while the efficiency of MHT alone is reduced compared to expectation due to particles confinement[71].

Unlike the case of gold and silver NPs for which it is known that PHT is due to plasmonic resonance under laser irradiation, the mechanism in the case of IO NPs and the parameters influencing the photothermal response are not clearly understood

View Article Online
DOI: 10.1039/D4NR01388C

yet. For example, Sadat *et al*. suggested that the heat generation is due to electronic transitions inside the IO lattice from the valence band to the conduction band[72]. Further, even if the mechanism and the parameters are still under debate, it seems that main parameters influencing PHT performances are not the size or shape but more precisely the quality of the crystallographic structure and the presence of defects (vacancies, dislocations, etc..) in the crystal structure. Indeed, in a previous work by Bertuit, Abou-Hassan and co-workers addressing the design of iron oxide nanoflowers having varying levels of defects, nanoflowers having excessive defects in terms of oxygen vacancies were found to decrease the photothermal effects. This was explained by the electrons trapping inside the structure decreasing the electron-heat conversion[73].

Given all this information, it seemed interesting to us to test the potential of our NPs for PHT therapies. The PHT properties of our IO@STMS-t NPs were thus evaluated using a NIR light irradiation at 1,064 nm. The NIR laser was applied to the different core-shell NPs suspensions at a fixed iron concentration (0.5 mgFe.mL^{-1}) and the temperature profiles were plotted and converted into SAR values using the mass of iron oxide as reference (**Figure 11**). Regarding the temperature profile, the final ΔT was found to be quite similar for the IO@STMS-t NPs from series 2, with a slight increase of the value between t=0 (*ca*. 23.1±0.4 °C) and t=40, 60 or 120 (*ca*. 25.2±0.2 °C, *ca*. 23.9±0.8 °C and *ca*. 23.8±0.1°C respectively) while a slight decrease of the values can be seen for the IO@STMS-t NPs from series 1 (*ca*. 21.9 °C versus *ca.* 19.1 °C, *ca.* 19.8 °C and *ca.* 19.4 °C, **Figure S15**). Taking these results in their globality, they mean that the thermal transfer is overall not affected by the large pore silica shell whatever the thickness.

The final SAR values were determined to be *ca.* 831±66 W.g^{-1} for IO@STMS-0 and *ca.* 1191±63 W.g^{-1}, *ca.* 1023±93 W.g^{-1} and *ca.* 1123±71 W.g^{-1} for IO@STMS-40, IO@STMS-60 and IO@STMS-120 respectively. Regarding the values obtained from series 1 (**Figure S15** and **Table S3**), the SAR value decreased slightly with the addition of the STMS shell and then with the growing of the STMS shell thickness (from
ca. 909 W.g^{-1} to *ca*. 712 W.g^{-1}). Taking again these results in their globality, it is difficult to really give a tendency for the impact of the STMS shell on the PHT properties of the IO NPs core as the values are quite similar whatever the particle series. Unfortunately, a standardisation of the SAR like the calculation of the ILP for

View Article Online
DOI: 10.1039/D4NR01388C

magnetothermal measurements is still unavailable for photothermal measurements, making the comparison of our values to the literature difficult. However, the high SAR values and the absence of clear impact of the silica shell on these SAR shows the promising aspect of the use of such NPs for PHT therapies.

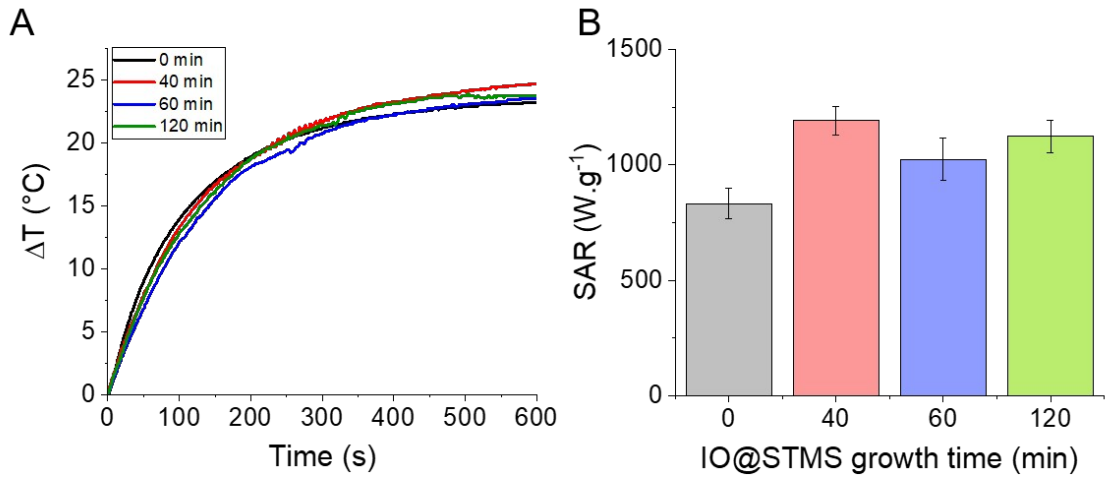

Figure 11: A) Temperature profiles as a function of time for the different IO@STMS-t NPs at 0.5 mgFe.mL^{-1} under NIR light irradiation. B) Corresponding SAR values. These results were obtained with the IO@STMS-t obtained from series 2.

III.5 Biological features: evaluation of NPs applicability to anti-cancer therapies

In the next sections, our goal was to evaluate the potential of our nanoparticles for anti-cancer therapies using magnetic fields as external stimuli. Thus, the pancreatic cancer cell line MiaPaca2 was chosen, as a model, to perform the *in vitro* experiments. In addition, as the STMS shell was added to the IO NPs core to counteract their rapid blood capillary agglomeration and elimination, IO NPs without STMS shell were not used for this study.

III.5.1 Cytotoxicity

The cytotoxicity of the IO@STMS-t NPs was first evaluated. To do so, MiaPaca2 cells were incubated for 24, 48 or 72 h with increased concentration of nanoparticles, based on the concentration of iron. Such decision was taken as we still wanted to see if we could see an impact of the STMS shell on the properties of the IO NPs core, and not only to determine if our NPs were good candidates for anti-cancer

View Article Online
DOI: 10.1039/D4NR01388C

therapies. The results presented in **Figure 12** clearly shows the higher cytotoxicity of IO@STMS-120 toward cells from early time points, compared to IO@STMS-40 and IO@STMS-60. The cytotoxicity of these IO@STMS-t (t=40 and 60) were still similar with always more than 90 % of survival after 24 h of incubation up to 100 µgFe.mL^{-1}. However, the IO@STMS-60 presented more cytotoxicity than IO@STMS-40 at 24 h and 48 h of incubation. Altogether, these results show that a concentration up to 0.78 µgFe.mL^{-1} of iron can be used for all IO@STMS-t NPs up to 72 h of incubation, as the final cell viability was *ca*. 90.37±4.80 % and *ca*. 90.50±2.17 % for IO@STMS-40 and IO@STMS-60 respectively, which is still very good, and *ca*. 82.15±2.99 % for IO@STMS-120, which is still acceptable. Thus, the non-cytotoxic concentration of 0.5 µgFe.mL^{-1} was chosen for the other experiments for all nanoparticles. In addition, in order to potentially increase efficiency of anti-cancer therapy using these nanoparticles and as the cytotoxicity of IO@STMS-40 and IO@STMS-60 are lower than IO@STMS-120 and still acceptable at 5 µgFe.mL^{-1}, we decided to test also this concentration with these two nanoparticles batches.

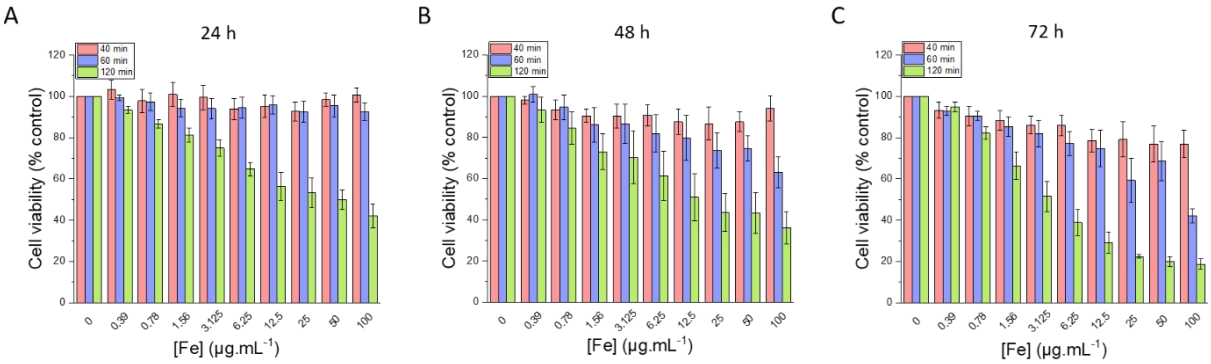

Figure 12: Cell viability evaluated after A) 24 h, B) 48 h and C) 72 h of incubation with different amount of IO@STMS-t NPs, with t=40, 60 or 120.

Regarding the chosen concentrations, to give some elements of comparison, in a previous work from our team[46], we previously evidenced an hyperthermia induced-cytotoxic effect on Hela cancer cells (*ca*. 65 % metabolic activity reduction vs control) under AMF using human serum albumin coated IO@STMS-120 at a concentration of 25 µgIO@STMS.mL^{-1} that corresponds to 1.25 µgFe.mL^{-1}. Field conditions providing cancer cell viability reduction were at 100 kHz and 357 Gauss (28.4 kA.m^{-1}) whose product is below the safety limit of H×f = 5 × 10^{9} Am^{-1}.s^{-1}, commonly admitted for localized hyperthermia[74]. Similarly, a concentration of 16 µgFe.mL^{-1} of IO NP coated

View Article Online
DOI: 10.1039/D4NR01388C

with PEG was shown to induce the death of different cancer cell lines (pancreatic, gastric cancer) by intra-lysosomal magnetic hyperthermia (AMF: 40 mT, 275 kHz)[75].

III.5.2 Cellular uptake

We then investigated the cellular uptake of the IO@STMS-t NPs. The cells were incubated for 72 h with IO@STMS-t NPs at a final concentration of 0.5 µgFe.mL^{-1} or 5 µgFe.mL^{-1}. As shown in **Figure 13.A**, the cellular uptake was ~ 0.04 pgFe.cell^{-1} and increased to ~ 0.4 pgFe.cell^{-1} when the cells were incubated respectively with 0.5 µgFe.mL^{-1} or 5 µgFe.mL^{-1} of IO@STMS-t NPs, indicating that the uptake proportionally increased, by 10-fold, with the concentration of IO@STMS-t NPs. These cellular uptakes corresponded respectively to *ca.* 13±5 %, 18±3 % and 21±3 % of the initial iron mass incubated of IO@STMS-40, IO@STMS-60 and IO@STMS-120 at 0.5 µgFe.mL^{-1} with the cells, suggesting a slight increase of the cellular uptake with the increase of the STMS shell thickness (**Figure 13.B**). However, our statistical test showed no significant difference between these values. In addition, similar percentages of the initial iron mass of IO@STMS-40 and IO@STMS-60, respectively *ca.* 14±4 % and *ca*. 14±2 %, were uptaken by cells incubated with 5 µgFe.mL^{-1}. Thus, we cannot conclude that the STMS shell has an impact on the cellular uptake of the NPs, as the values are quite close.

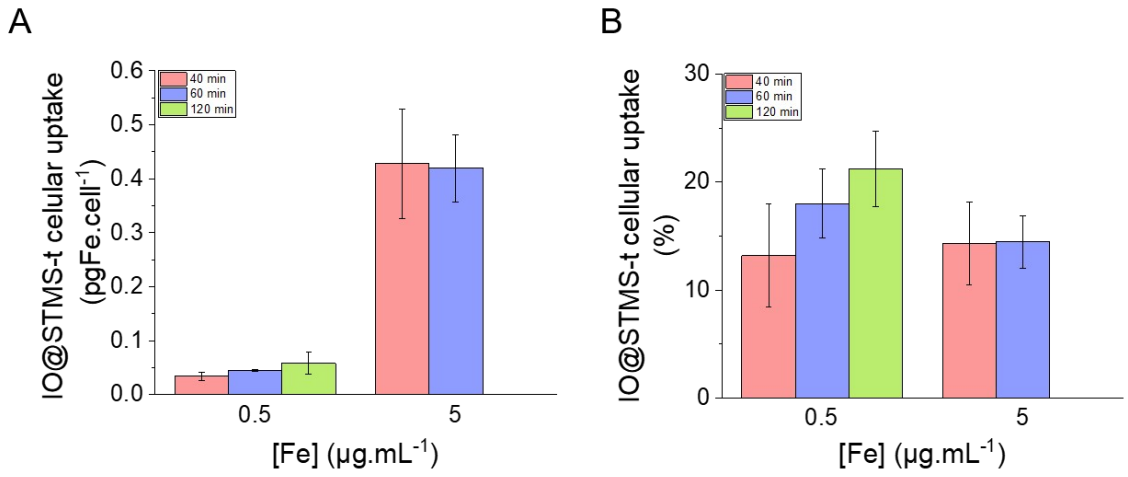

Figure 13: IO@STMS-t NPs cellular uptake in A) pgFe.cell^{-1} and in B) percentage of incubated iron. Statistical analysis gave no significant difference between the groups.

View Article Online
DOI: 10.1039/D4NR01388C

TEM was also performed on the samples incubated at 5 µgFe.mL^{-1} for 72 h in order to investigate the particles localization inside the cells. As it can be seen in **Figure 14**, the particles are localized in the lysosomes, meaning that we would have endo-lysosomal hyperthermia under AMF.

Another interesting result obtained from this TEM intracellular imaging is that the silica shell appear to be importantly intracellularly degraded as only clustered IO NPs can be seen on the images presented in **Figure 14**. However, it is important to note that silica shells could still be observed in very few imaged areas of IO@STMS-60 and IO@STMS-120. Indeed, as it can be seen in **Figure S16.A**, some IO NPs are not all clustered in the case of IO@STMS-60 and present a kind of corona that might be the silica shell degrading, being more transparent to the electron beam, leading thus to this poor contrast. However, the silica shell is clearly observable in the case of IO@STMS-120 as shown in **Figure S16.B**.

The intracellular degradation of mesoporous silica NPs and also of iron oxide clusters@mesoporous silica NPs were previously reported to occur from some days to several weeks depending on the different parameters influencing the silica dissolution: NPs concentration (silica limit solubility is 140-160 µg.mL^{-1}) under standard physiological conditions (37 ° C, pH 7.2), NPs aggregation state, pore size, degree of silica condensation, etc…[37,76]

In our case, TEM intracellular imaging suggests that the degradation of the silica shell in the lysosomes is occurring rapidly (in three days) and is heterogeneous, which can come from the fact that the particle concentration is quite low providing suitable low intra-lysosomal confinement and thus favouring silica shell dissolution.

View Article Online
DOI: 10.1039/D4NR01388C

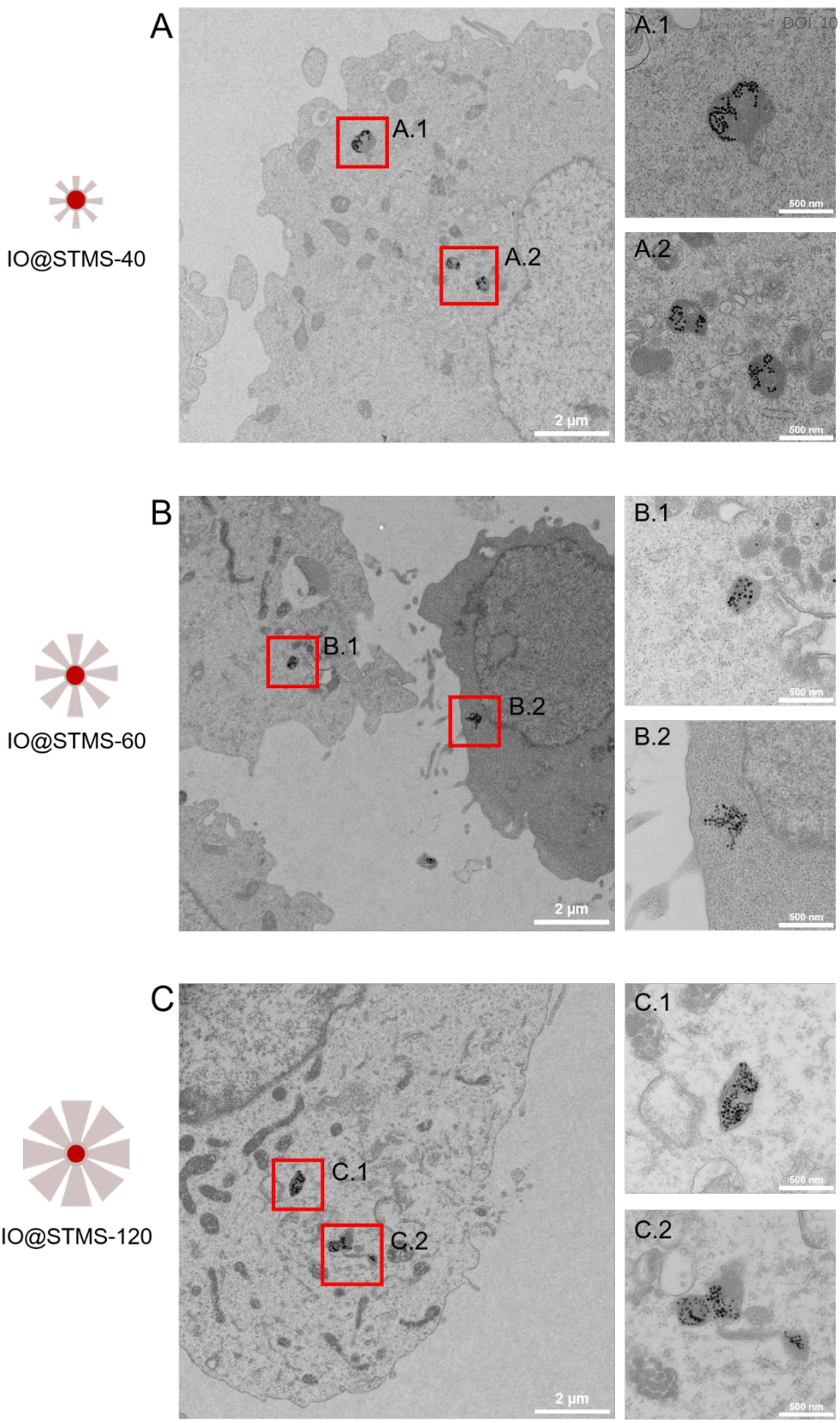

Figure 14: TEM images of cells incubated at 5 µgFe.mL^{-1} for 72 h with A) IO@STMS-40, B) IO@STMS-60 and C) IO@STMS-120 and respective magnifications of lysosomes in A.1, A.2; B.1, B.2 and C.1, C.2.

View Article Online
DOI: 10.1039/D4NR01388C

III.5.3 Cytotoxicity under magnetic stimuli

The applicability to anti-cancer therapies using external stimuli was then studied. The cells were incubated or not with the IO@STMS-t NPs to allow their internalization, then exposed or not to an AMF with a frequency f of 250 kHz and an amplitude H of 20 mT (16 $kA.m^{-1}$) for 2 h. The cells that were not incubated with NPs *and* not submitted to AMF served as control to evaluate the efficiency of the treatment. The cell death was then evaluated using Annexin V (AnnV) and Propidium Iodide (PI) labelling. Such labelling was chosen in order to give a first insight on the mechanism of the cell death. Indeed, the AnnV is a marker of early apoptosis, as it binds to certain phospholipids that normally face the interior of the cell (in contact with the cytoplasm) but face the exterior of the cells (in contact with the environment) in the early stages of apoptosis. Regarding PI, this molecule is a marker of necrosis, as it binds to DNA and can enter the cells only if the membrane becomes more permeable. The case where both molecules label the same cell corresponds more to late apoptotic cell death. However, it has to be kept in mind that this technique gives insight on the cell death mechanism, but that more specific tests should be performed to discriminate, for example, primary necrotic cell death from late apoptotic cell death[77]. In the case of anti-cancer therapies, a cell death mechanism by apoptosis is highly researched as it corresponds to a programmed suicide of the cell in response to the treatment without the release of detrimental molecules for other cells, while cell death by necrosis is an accidental cell death leading to the release of such molecules.

The results of this labelling is presented in **Figure 15**. As expected, the incubation of the cells with the NPs only did not significantly increase cell death compared to the control, as well as the treatment with AMF only. Interestingly, the AMF exposure increased the mortality of MiaPaca2 cancer cells incubated with IO@STMS-40, especially at 5 $\mu gFe.mL^{-1}$. Indeed, the cell death was increased only from *ca*. 11.2±1.5 %, *ca*. 13.6±2.2 % and *ca*. 9.1±1.2 % for the control, NPs only and AMF only respectively to *ca*. 17.3±0.6 % for AMF+NPs when the cells were incubated at 0.5 $\mu gFe.mL^{-1}$ while it went up to *ca*. 28.8±2.3 % when the cells were incubated at 5 $\mu gFe.mL^{-1}$, which was determined to be significantly higher than the % of dead cells measured for the other treatment. Moreover, dead cells are mainly labelled by AnnV, indicating an apoptosis related cell death pathway induced by IO@STMS-40

View Article Online
DOI: 10.1039/D4NR01388C

upon MHT treatment. In contrast, IO@STMS-60 and IO@STMS-120 did not decrease the viability of MiaPaca2 cancer cells upon MHT treatment.

Regarding these magnetothermal effects under AMF, we can only speculate that the improved cancer cell killing with IO@STMS-40 sample as compared to others samples is due to local heating effects at the surface of the IO NPs through the silica large pore shell. Even if both of the AMF treatments on IO@STMS-t are made in macroscopically athermic conditions, we can hypothesize that the local temperature is higher when the silica shell is lower and more opened. For instance, several teams showed a huge reduction in cancer cell viability using targeted magnetic nanoparticles without the need for a perceptible temperature rise[75,78,79]. Further, the total absence of silica shell observed by the above intra-cellular TEM imaging in IO@STMS-40 as compared to IOSTMS-60 may also play a role in local related effects at iron oxide surface (magnetothermal effect, ROS production, etc..) and thus might contribute in improving cytotoxicity.

Thus, these results tend to show that even if the IO@STMS-40 has lower SAR values, at a slightly lower or similar amount of internalized iron, they are still the more promising nanoparticles for anti-cancer therapies using AMF.

View Article Online
DOI: 10.1039/D4NR01388C

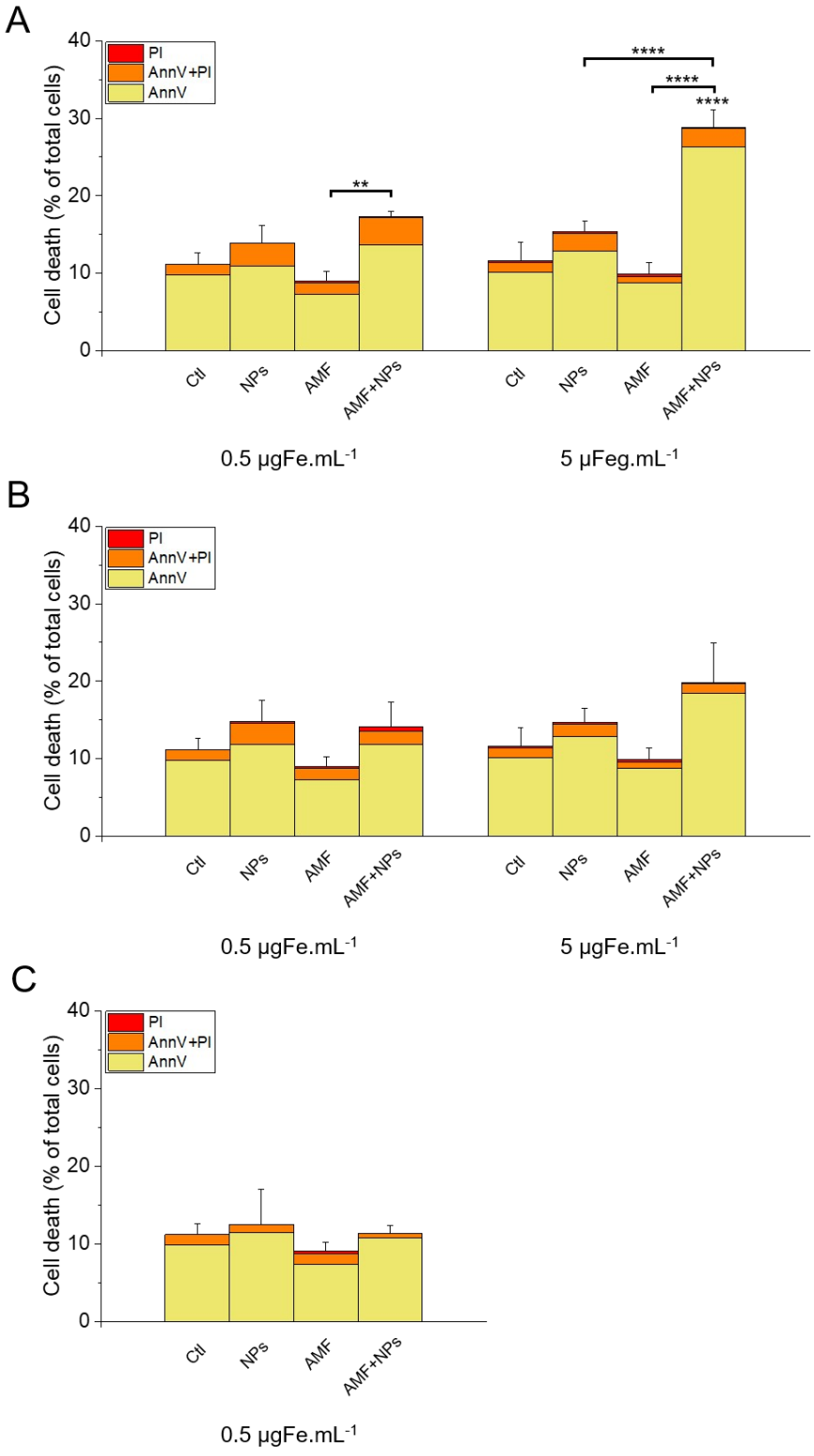

Figure 15: Cell death evaluated in presence or absence of IO@STMS-t NPs with or without AMF stimulus for A) IO@STMS-40, B) IO@STMS-60 and C) IO@STMS-120. Error bars are on the total percentage as well as the statistical analysis.

View Article Online
DOI: 10.1039/D4NR01388C

IO@STMS-40 NPs were thus used for a complementary experiment analysing the cell proliferation. The cells were incubated or not with these NPs at 5 µgFe.mL^{-1} for 72 h and exposed respectively one, two or three times to AMF (or not). A schematic representation of the protocol is given in **Figure 16.A** to better perceive it. The results, presented in **Figure 16.B**, shows that the cell proliferation is affected over time under exposure to AMF, and even more under exposure to AMF after being incubated with cells. Indeed, the number of cells dropped from $5.6\times10^5 \pm 3.0\times10^4$ without NPs or AMF, to $4.9\times10^5 \pm 3.9\times10^4$ after three exposures to AMF and to $3.8\times10^5 \pm 2.8\times10^4$ after incubation with NPs and three exposures to AMF, which has been determined to be significantly different as shown in **Figure 16.C**. These results show again that IO@STMS-40 are promising NPs for anti-cancer therapies using AMF.

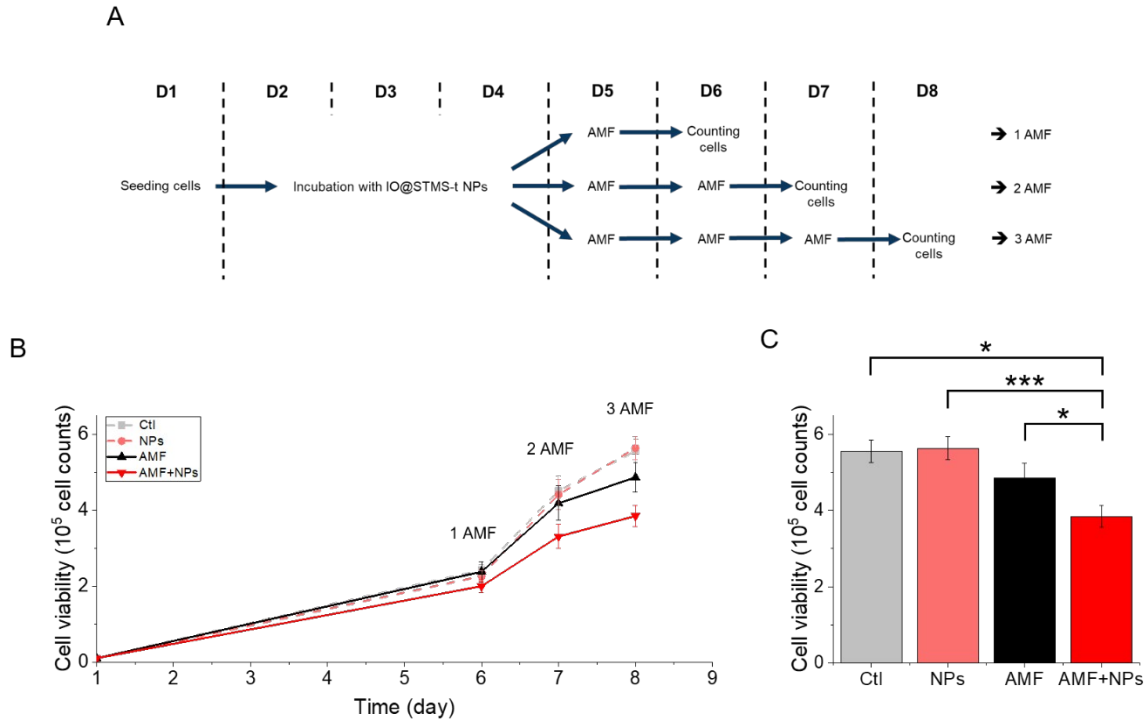

Figure 16: A) Schematic representation of the applied protocol. B) Proliferation of MiaPaca2 cancer cells along the treatment. Statistical analysis was done on the C) proliferation at day 8.

The application of an AMF to evaluate the potential of IO@STMS-t NPs for anti-cancer therapies makes sense as these particles are studied for magnetic hyperthermia treatment. However, it is also possible to use RMF in order to see if the

View Article Online
DOI: 10.1039/D4NR01388C

NPs can induce cell death by mechanical forces and not only by the local increase of the temperature. Similar experiments were then performed upon RMF application, with a frequency f of 1 Hz and an amplitude H of 40 mT (32 $kA.m^{-1}$). As it can be seen on **Figure 17**, only 5 $\mu gFe.mL^{-1}$ of IO@STMS-40 increased significantly the cell death:

ca. 22.6±2.3 % comparatively to *ca.* 11.2±1.5 % of control cells. Moreover, dead cells are also mainly labelled by AnnV, indicating an apoptosis related cell death pathway induced by IO@STMS-40 motion upon RMF application. Regarding these RMF results, we could also hypothesize that the NPs chaining is more probable with lower silica shell and may induce more efficient torque effects for IO@STMS-40 as compared to IO@STMS-60. However, these nanoparticles seemed less efficient under RMF compared to AMF: *ca*. 22.6±2.3 % versus *ca*. 28.8±2.3 % of cell death respectively after 5 $\mu gFe.mL^{-1}$ of IO@STMS-40 incubation.

Regarding the multiple application of RMF with or without IO@STMS-40 NPs, which results are presented in **Figure 18**, they show a significant impact of the multiple exposure to RMF and to RMF with NPs. Indeed, the number of cells dropped from $5.6\times10^5 \pm 3.0\times10^4$ without NPs or RMF, to $4.8\times10^5 \pm 3.1\times10^4$ after three exposures to RMF and to $3.8\times10^5 \pm 2.3\times10^4$ after incubation with NPs and three exposures to RMF, showing one more time the great potential of IO@STMS-40 NPs for anti-cancer therapy under RMF.

View Article Online
DOI: 10.1039/D4NR01388C

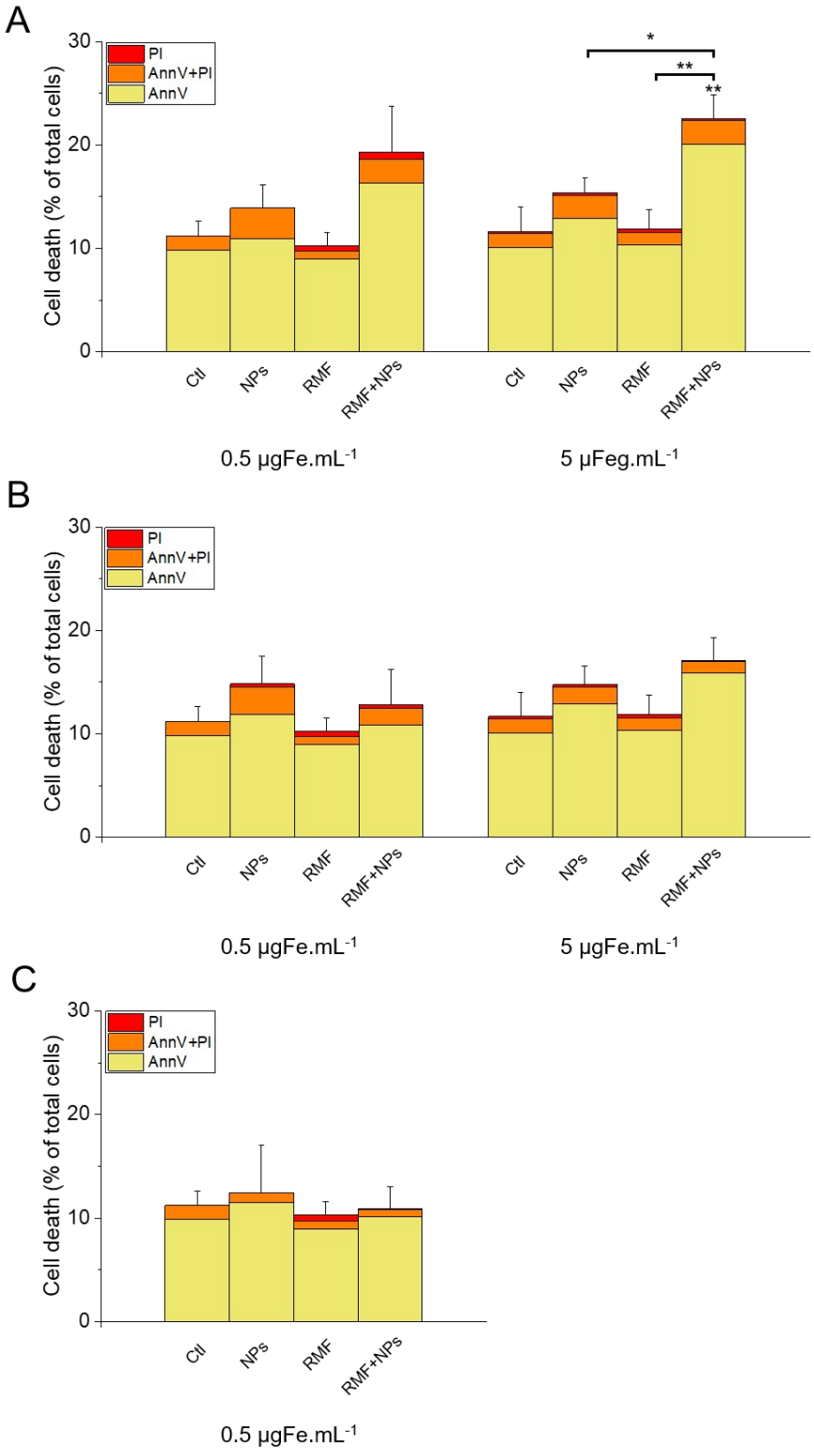

Figure 17: Cell death evaluated in presence or absence of IO@STMS-t NPs with or without RMF stimulus for A) IO@STMS-40, B) IO@STMS-60 and C) IO@STMS-120. Error bars are on the total percentage as well as the statistical analysis.

View Article Online
DOI: 10.1039/D4NR01388C

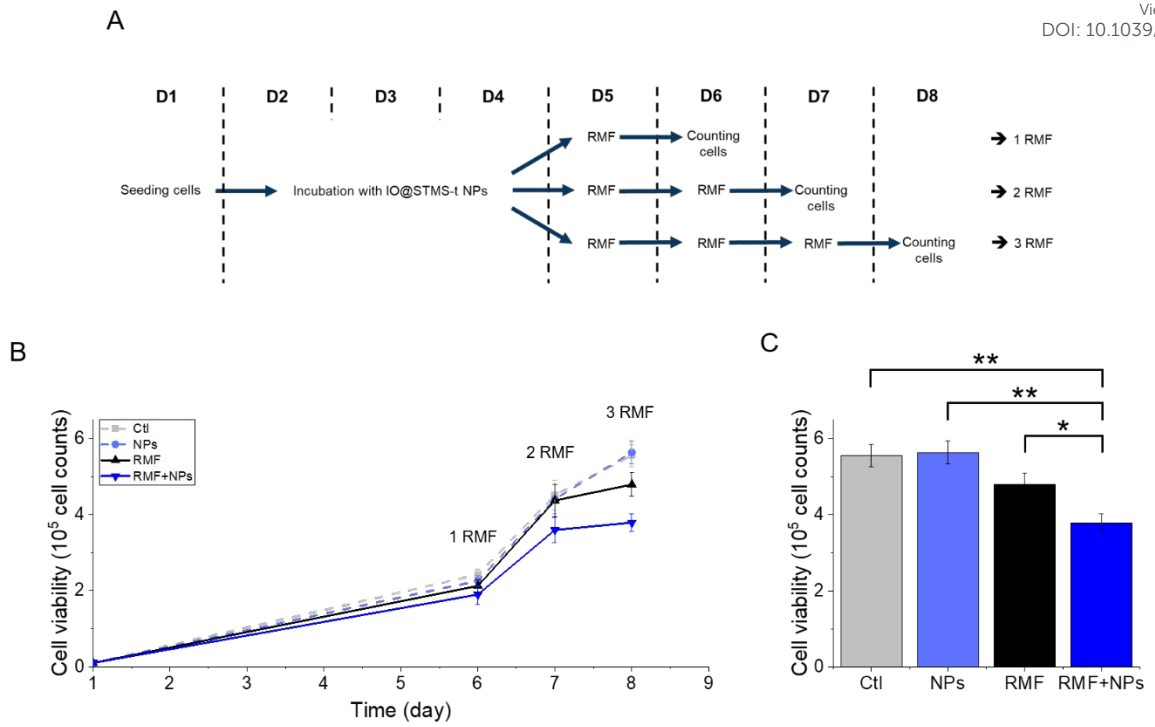

Figure 18: A) Proliferation of MiaPaca2 cancer cells along the treatment. Statistical analysis was done on the B) proliferation at day 8 after three exposures to RMF or no exposure.

Altogether, these results show that IO@STMS-40 are the best candidate between the IO@STMS-t NPs for anti-cancer therapies, whether using AMF or RMF stimulus. The cell death may represent a low value (~ 23-29 % of total cells), which can be disappointing regarding the quite high SAR and ILP values determined in the previous section. However, the multiple exposure to AMF or RMF significantly reduced cell proliferation, showing its potential for such application.

In addition, we have to keep in mind that the IO@STMS-t NPs were used here without any polymer coating. Such coating may enhance their internalization and decrease cytotoxicity which would allow to increase the concentration of nanoparticles, and thus should increase their anti-cancer efficiency.

As a perspective, there are various strategies of polymer coatings around mesoporous silica that may be used to enhance cancer cell uptake. Among them, we can cite polycation surface modifications like the non-covalently adsorbed polyethyleneimine coatings ensuring strong interaction with the negatively charged cell membrane, and yielding to high cellular uptake[80]. We can cite also the covalently bound polyarginine acting as a cancer cell penetrating cationic polypeptide[81]. Another

View Article Online
DOI: 10.1039/D4NR01388C

surface modification strategy is the covalent conjugation of hyaluronic acid, a negatively charged polyelectrolyte, which ensures the efficient cell internalization though targeting with CD44 receptor overexpressed in cancer cells[82].

IV Conclusion

In this work, we have addressed the fine tuning of the STMS shell growth around IO NPs core by simply playing on the sol-gel time of the synthesis. The control of the STMS shell growth was evidenced as well by time-lapse TEM imaging as by *in situ* LPTEM which were found to be very complementary. Evolution of the pore structure was also deeply investigated by nitrogen adsorption-desorption measurements (BET, BJH and Horvarth-Kawazoe methods) and we could show that increasing the shell thickness resulted in decreasing the specific surface area, the pore volume and pore size. This new synthesis approach based on a very simple procedure allows to afford a range of new IO@STMS core-shell NPs with tunable shell thickness, and pore structure. Further, all of these IO@STMS-t (with t being the growth time) were shown to have overall a good colloidal stability.

The impact of the STMS shell thickness on the MRI and hyperthermia properties of the IO NPs core were then studied. First, regarding MRI applications, we showed that the STMS shell growth had no detrimental impact on the T_2-weighted MRI relaxivities making these IO@STMS-t NPs very good T_2 contrast agents with relaxivity values in the range of 320-377 $mM^{-1}.s^{-1}$. Regarding evolution of the T_1-weighted MRI relaxivities which decreased strongly with silica shell thicknesses, they allow to confirm the densification of the silica walls with the increase of the time growth, limiting water accessibility. Regarding the hyperthermia properties of the IO@STMS-t NPs, we could see a slight decrease of the SAR value determined under AMF stimulus and no clear impact on the SAR value determined under NIR light stimulus, indicating that the stellate porous silica shell provides a low insulating property with silica shell growth. Overall, it does not affect the heat dissipation from the core to the surrounding media making all these core-shell IO@STMS-t NPs efficient heating agents under AMF or NIR light irradiation stimulation.

Finally, several *in vitro* experiments using the pancreatic cancer cell line MiaPaca2 were performed in order to evaluate the potential use of these IO@STMS-t NPs for anti-cancer applications. We could show that ~ 14 % of the incubated particles were

View Article Online
DOI: 10.1039/D4NR01388C

internalised by the cells and that the application of AMF or RMF improved the anti-cancer efficiency of IO@STMS-40.

This study showed the great interest of adding the STMS shell around the IO NPs core as it notably stabilises the particles and does not hinder its interesting properties, namely MRI, MHT and PHT. In addition, the *in vitro* experiments showed the interest of using such core-shell NPs to improve anti-cancer treatment by using external magnetic fields. Such systems could then be envisioned for bimodal anti-cancer application, with the combination of local hyperthermia with the thermally-induced controlled delivery of therapeutic molecules of higher size than synthesised ones, such as protein, DNA or RNA. However, such biomolecules being quite sensitive to thermal denaturation, evaluation of the local temperature at the surface of the IO@STMS NPs would also be future studies to investigate.

Conflict of Interests. There are no conflicts of interest to declare.

Acknowledgments. D.M. and J.B. (for PhD and postdoc supports) acknowledge the Agence Nationale de la Recherche (grant ANR-19-CE09-0004—Corelmag) and the Materials Institute Carnot Alsace (Inter-Carnot project, Nanobiocities). The spectroscopy and the transmission electronic microscopy platforms of the IPCMS are acknowledged for technical supports.

View Article Online
DOI: 10.1039/D4NR01388C

V References

(1) Choi, K. Y.; Liu, G.; Lee, S.; Chen, X. Theranostic Nanoplatforms for Simultaneous Cancer Imaging and Therapy: Current Approaches and Future Perspectives. *Nanoscale* **2012**, *4* (2), 330–342. https://doi.org/10.1039/C1NR11277E.

(2) Janib, S. M.; Moses, A. S.; MacKay, J. A. Imaging and Drug Delivery Using Theranostic Nanoparticles. *Advanced Drug Delivery Reviews* **2010**, *62* (11), 1052–1063. https://doi.org/10.1016/j.addr.2010.08.004.

(3) Blanco-Andujar, C.; Walter, A.; Cotin, G.; Bordeianu, C.; Mertz, D.; Felder-Flesch, D.; Begin-Colin, S. Design of Iron Oxide-Based Nanoparticles for MRI and Magnetic Hyperthermia. *Nanomedicine (Lond)* **2016**, *11* (14), 1889–1910. https://doi.org/10.2217/nnm-2016-5001.

(4) Laurent, S.; Forge, D.; Port, M.; Roch, A.; Robic, C.; Vander Elst, L.; Muller, R. N. Magnetic Iron Oxide Nanoparticles: Synthesis, Stabilization, Vectorization, Physicochemical Characterizations, and Biological Applications. *Chem. Rev.* **2008**, *108* (6), 2064–2110. https://doi.org/10.1021/cr068445e.

(5) Na, H. B.; Song, I. C.; Hyeon, T. Inorganic Nanoparticles for MRI Contrast Agents. *Adv. Mater.* **2009**, *21* (21), 2133–2148. https://doi.org/10.1002/adma.200802366.

(6) Hachani, R.; Lowdell, M.; Birchall, M.; Hervault, A.; Mertz, D.; Begin-Colin, S.; Thanh, N. T. K. Polyol Synthesis, Functionalisation, and Biocompatibility Studies of Superparamagnetic Iron Oxide Nanoparticles as Potential MRI Contrast Agents. *Nanoscale* **2016**, *8* (6), 3278–3287. https://doi.org/10.1039/C5NR03867G.

(7) Thiesen, B.; Jordan, A. Clinical Applications of Magnetic Nanoparticles for Hyperthermia. *International Journal of Hyperthermia* **2008**, *24* (6), 467–474. https://doi.org/10.1080/02656730802104757.

(8) Maier-Hauff, K.; Ulrich, F.; Nestler, D.; Niehoff, H.; Wust, P.; Thiesen, B.; Orawa, H.; Budach, V.; Jordan, A. Efficacy and Safety of Intratumoral Thermotherapy Using Magnetic Iron-Oxide Nanoparticles Combined with External Beam Radiotherapy on Patients with Recurrent Glioblastoma Multiforme. *J Neurooncol* **2011**, *103* (2), 317–324. https://doi.org/10.1007/s11060-010-0389-0.

(9) Maier-Hauff, K.; Rothe, R.; Scholz, R.; Gneveckow, U.; Wust, P.; Thiesen, B.; Feussner, A.; von Deimling, A.; Waldoefner, N.; Felix, R.; Jordan, A. Intracranial Thermotherapy Using Magnetic Nanoparticles Combined with External Beam Radiotherapy: Results of a Feasibility Study on Patients with Glioblastoma Multiforme. *J Neurooncol* **2007**, *81* (1), 53–60. https://doi.org/10.1007/s11060-006-9195-0.

(10) Freis, B.; Cotin, G.; Perton, F.; Mertz, D.; Boutry, S.; Laurent, S.; Begin-Colin, S. The Size, Shape, and Composition Design of Iron Oxide Nanoparticles to Combine, MRI, Magnetic Hyperthermia, and Photothermia. In *Magnetic Nanoparticles in Human Health and Medicine*; Caizer, C., Rai, M., Eds.; Wiley, 2021; pp 380–429. https://doi.org/10.1002/9781119754725.ch17.

(11) Estelrich, J.; Busquets, M. Iron Oxide Nanoparticles in Photothermal Therapy. *Molecules* **2018**, *23* (7), 1567. https://doi.org/10.3390/molecules23071567.

(12) Shen, S.; Wang, S.; Zheng, R.; Zhu, X.; Jiang, X.; Fu, D.; Yang, W. Magnetic Nanoparticle Clusters for Photothermal Therapy with Near-Infrared Irradiation. *Biomaterials* **2015**, *39*, 67–74. https://doi.org/10.1016/j.biomaterials.2014.10.064.

(13) Cabana, S.; Curcio, A.; Michel, A.; Wilhelm, C.; Abou-Hassan, A. Iron Oxide Mediated Photothermal Therapy in the Second Biological Window: A Comparative Study between Magnetite/Maghemite Nanospheres and Nanoflowers. *Nanomaterials* **2020**, *10* (8), 1548. https://doi.org/10.3390/nano10081548.

(14) Yu, T.-J.; Li, P.-H.; Tseng, T.-W.; Chen, Y.-C. Multifunctional Fe_3O_4 /Alumina Core/Shell MNPs as Photothermal Agents for Targeted Hyperthermia of Nosocomial and Antibiotic-Resistant Bacteria. *Nanomedicine* **2011**, *6* (8), 1353–1363. https://doi.org/10.2217/nnm.11.34.

(15) Mahmoudi, M.; Lynch, I.; Ejtehadi, M. R.; Monopoli, M. P.; Bombelli, F. B.; Laurent, S. Protein−Nanoparticle Interactions: Opportunities and Challenges. *Chem. Rev.* **2011**, *111* (9), 5610–5637. https://doi.org/10.1021/cr100440g.

(16) Cotin, G.; Piant, S.; Mertz, D.; Felder-Flesch, D.; Begin-Colin, S. Iron Oxide Nanoparticles for Biomedical Applications: Synthesis, Functionalization, and Application. In *Iron Oxide Nanoparticles for Biomedical Applications : Synthesis, Functionalization, and Application*; Elsevier, 2018; pp 43–88. https://doi.org/10.1016/B978-0-08-101925-2.00002-4.

(17) Manzano, M.; Vallet-Regí, M. Mesoporous Silica Nanoparticles for Drug Delivery. *Adv. Funct. Mater.* **2020**, *30* (2), 1902634. https://doi.org/10.1002/adfm.201902634.

(18) Tang, F.; Li, L.; Chen, D. Mesoporous Silica Nanoparticles: Synthesis, Biocompatibility and Drug Delivery. *Adv. Mater.* **2012**, *24* (12), 1504–1534. https://doi.org/10.1002/adma.201104763.

(19) Argyo, C.; Weiss, V.; Bräuchle, C.; Bein, T. Multifunctional Mesoporous Silica Nanoparticles as a Universal Platform for Drug Delivery. *Chem. Mater.* **2014**, *26* (1), 435–451. https://doi.org/10.1021/cm402592t.

(20) Kim, J.; Kim, H. S.; Lee, N.; Kim, T.; Kim, H.; Yu, T.; Song, I. C.; Moon, W. K.; Hyeon, T. Multifunctional Uniform Nanoparticles Composed of a Magnetite Nanocrystal Core and a Mesoporous Silica Shell for Magnetic Resonance and Fluorescence Imaging and for Drug Delivery. *Angewandte Chemie International Edition* **2008**, *47* (44), 8438–8441. https://doi.org/10.1002/anie.200802469.

(21) Liu, J.; Detrembleur, C.; De Pauw-Gillet, M.-C.; Mornet, S.; Elst, L. V.; Laurent, S.; Jérôme, C.; Duguet, E. Heat-Triggered Drug Release Systems Based on Mesoporous Silica Nanoparticles Filled with a Maghemite Core and Phase-Change Molecules as Gatekeepers. *J. Mater. Chem. B* **2014**, *2* (1), 59–70. https://doi.org/10.1039/C3TB21229G.

(22) Knežević, N. Ž.; Slowing, I. I.; Lin, V. S.-Y. Tuning the Release of Anticancer Drugs from Magnetic Iron Oxide/Mesoporous Silica Core/Shell Nanoparticles. *ChemPlusChem* **2012**, *77* (1), 48–55. https://doi.org/10.1002/cplu.201100026.

(23) Asgari, M.; Soleymani, M.; Miri, T.; Barati, A. A Robust Method for Fabrication of Monodisperse Magnetic Mesoporous Silica Nanoparticles with Core-Shell Structure as Anticancer Drug Carriers. *Journal of Molecular Liquids* **2019**, *292*, 111367. https://doi.org/10.1016/j.molliq.2019.111367.

(24) Yang, P.; Gai, S.; Lin, J. Functionalized Mesoporous Silica Materials for Controlled Drug Delivery. *Chemical Society Reviews* **2012**, *41* (9), 3679. https://doi.org/10.1039/c2cs15308d.

(25) Deng, Y.; Qi, D.; Deng, C.; Zhang, X.; Zhao, D. Superparamagnetic High-Magnetization Microspheres with an Fe_3O_4 @SiO_2 Core and Perpendicularly Aligned Mesoporous SiO_2 Shell for Removal of Microcystins. *Journal of the*

American Chemical Society **2008**, *130* (1), 28–29. https://doi.org/10.1021/ja0777584.

(26) Kim, J.; Lee, J. E.; Lee, J.; Yu, J. H.; Kim, B. C.; An, K.; Hwang, Y.; Shin, C.-H.; Park, J.-G.; Kim, J.; Hyeon, T. Magnetic Fluorescent Delivery Vehicle Using Uniform Mesoporous Silica Spheres Embedded with Monodisperse Magnetic and Semiconductor Nanocrystals. *Journal of the American Chemical Society* **2006**, *128* (3), 688–689. https://doi.org/10.1021/ja0565875.

(27) Fan, H.; Yang, K.; Boye, D. M.; Sigmon, T.; Malloy, K. J.; Xu, H.; López, G. P.; Brinker, C. J. Self-Assembly of Ordered, Robust, Three-Dimensional Gold Nanocrystal/Silica Arrays. *Science* **2004**, *304* (5670), 567–571. https://doi.org/10.1126/science.1095140.

(28) Fan, H.; Leve, E. W.; Scullin, C.; Gabaldon, J.; Tallant, D.; Bunge, S.; Boyle, T.; Wilson, M. C.; Brinker, C. J. Surfactant-Assisted Synthesis of Water-Soluble and Biocompatible Semiconductor Quantum Dot Micelles. *Nano Letters* **2005**, *5* (4), 645–648. https://doi.org/10.1021/nl050017l.

(29) Fan, H.; Chen, Z.; Brinker, C. J.; Clawson, J.; Alam, T. Synthesis of Organo-Silane Functionalized Nanocrystal Micelles and Their Self-Assembly. *Journal of the American Chemical Society* **2005**, *127* (40), 13746–13747. https://doi.org/10.1021/ja053795o.

(30) Fan, H.; Wright, A.; Gabaldon, J.; Rodriguez, A.; Brinker, C. J.; Jiang, Y.-B. Three-Dimensionally Ordered Gold Nanocrystal/Silica Superlattice Thin Films Synthesized via Sol–Gel Self-Assembly. *Advanced Functional Materials* **2006**, *16* (7), 891–895. https://doi.org/10.1002/adfm.200500603.

(31) Ye, F.; Laurent, S.; Fornara, A.; Astolfi, L.; Qin, J.; Roch, A.; Martini, A.; Toprak, M. S.; Muller, R. N.; Muhammed, M. Uniform Mesoporous Silica Coated Iron Oxide Nanoparticles as a Highly Efficient, Nontoxic MRI T2 Contrast Agent with Tunable Proton Relaxivities: Fe3O4@mSiO2 WITH TUNABLE RELAXIVITIES. *Contrast Media & Molecular Imaging* **2012**, *7* (5), 460–468. https://doi.org/10.1002/cmmi.1473.

(32) Bizeau, J.; Mertz, D. Design and Applications of Protein Delivery Systems in Nanomedicine and Tissue Engineering. *Advances in Colloid and Interface Science* **2021**, *287*, 102334. https://doi.org/10.1016/j.cis.2020.102334.

(33) Zhang, J.; Li, X.; Rosenholm, J. M.; Gu, H. Synthesis and Characterization of Pore Size-Tunable Magnetic Mesoporous Silica Nanoparticles. *Journal of Colloid and Interface Science* **2011**, *361* (1), 16–24. https://doi.org/10.1016/j.jcis.2011.05.038.

(34) Sun, Z.; Zhou, X.; Luo, W.; Yue, Q.; Zhang, Y.; Cheng, X.; Li, W.; Kong, B.; Deng, Y.; Zhao, D. Interfacial Engineering of Magnetic Particles with Porous Shells: Towards Magnetic Core – Porous Shell Microparticles. *Nano Today* **2016**, *11* (4), 464–482. https://doi.org/10.1016/j.nantod.2016.07.003.

(35) Xiong, L.; Bi, J.; Tang, Y.; Qiao, S. Magnetic Core–Shell Silica Nanoparticles with Large Radial Mesopores for SiRNA Delivery. *Small* **2016**, *12* (34), 4735–4742. https://doi.org/10.1002/smll.201600531.

(36) Nemec, S.; Kralj, S. A Versatile Interfacial Coassembly Method for Fabrication of Tunable Silica Shells with Radially Aligned Dual Mesopores on Diverse Magnetic Core Nanoparticles. *ACS Appl. Mater. Interfaces* **2021**, *13* (1), 1883–1894. https://doi.org/10.1021/acsami.0c17863.

(37) Fiedler, R.; Sivakumaran, G.; Mallén, J.; Lindén, M. Superparamagnetic Core–Mesoporous Silica Shell Nanoparticles with Tunable Extra- and Intracellular

Dissolution Rates. *Chemistry of Materials* **2024**, *36* (6), 2790–2798. https://doi.org/10.1021/acs.chemmater.3c02986.

(38) Fiedler, R.; Beizinger, B.; Walther, P.; Lindén, M. Synthesis of Highly Monodisperse Superparamagnetic Iron Oxide Core@mesoporous Silica Shell Particles with Independently Tunable Size, and Porosity. *Microporous and Mesoporous Materials* **2022**, *340*, 112027. https://doi.org/10.1016/j.micromeso.2022.112027.

(39) Zhang, K.; Xu, L.-L.; Jiang, J.-G.; Calin, N.; Lam, K.-F.; Zhang, S.-J.; Wu, H.-H.; Wu, G.-D.; Albela, B.; Bonneviot, L.; Wu, P. Facile Large-Scale Synthesis of Monodisperse Mesoporous Silica Nanospheres with Tunable Pore Structure. *J. Am. Chem. Soc.* **2013**, *135* (7), 2427–2430. https://doi.org/10.1021/ja3116873.

(40) Perton, F.; Harlepp, S.; Follain, G.; Parkhomenko, K.; Goetz, J. G.; Bégin-Colin, S.; Mertz, D. Wrapped Stellate Silica Nanocomposites as Biocompatible Luminescent Nanoplatforms Assessed in Vivo. *Journal of Colloid and Interface Science* **2019**, *542*, 469–482. https://doi.org/10.1016/j.jcis.2019.01.098.

(41) Duenas-Ramirez, P.; Bertagnolli, C.; Müller, R.; Sartori, K.; Boos, A.; Elhabiri, M.; Bégin-Colin, S.; Mertz, D. Highly Chelating Stellate Mesoporous Silica Nanoparticles for Specific Iron Removal from Biological Media. *Journal of Colloid and Interface Science* **2020**, *579*, 140–151. https://doi.org/10.1016/j.jcis.2020.06.013.

(42) Bizeau, J.; Adam, A.; Nadal, C.; Francius, G.; Siniscalco, D.; Pauly, M.; Bégin-Colin, S.; Mertz, D. Protein Sustained Release from Isobutyramide-Grafted Stellate Mesoporous Silica Nanoparticles. *International Journal of Pharmaceutics: X* **2022**, *4*, 100130. https://doi.org/10.1016/j.ijpx.2022.100130.

(43) Bizeau, J.; Adam, A.; Bégin, S.; Mertz, D. Serum Albumin Antifouling Effects of Hydroxypropyl-cellulose and Pluronic F127 Adsorbed on Isobutyramide-grafted Stellate Silica Nanoparticles. *Eur. J. Inorg. Chem.* **2021**, ejic.202100678. https://doi.org/10.1002/ejic.202100678.

(44) Adam, A.; Parkhomenko, K.; Duenas-Ramirez, P.; Nadal, C.; Cotin, G.; Zorn, P.-E.; Choquet, P.; Bégin-Colin, S.; Mertz, D. Orienting the Pore Morphology of Core-Shell Magnetic Mesoporous Silica with the Sol-Gel Temperature. Influence on MRI and Magnetic Hyperthermia Properties. *Molecules* **2021**, *26* (4), 971. https://doi.org/10.3390/molecules26040971.

(45) Adam, A.; Harlepp, S.; Ghilini, F.; Cotin, G.; Freis, B.; Goetz, J.; Bégin, S.; Tasso, M.; Mertz, D. Core-Shell Iron Oxide@stellate Mesoporous Silica for Combined near-Infrared Photothermia and Drug Delivery: Influence of PH and Surface Chemistry. *Colloids and Surfaces A: Physicochemical and Engineering Aspects* **2022**, *640*, 128407. https://doi.org/10.1016/j.colsurfa.2022.128407.

(46) Perton, F.; Tasso, M.; Muñoz Medina, G. A.; Ménard, M.; Blanco-Andujar, C.; Portiansky, E.; van Raap, M. B. F.; Bégin, D.; Meyer, F.; Begin-Colin, S.; Mertz, D. Fluorescent and Magnetic Stellate Mesoporous Silica for Bimodal Imaging and Magnetic Hyperthermia. *Applied Materials Today* **2019**, *16*, 301–314. https://doi.org/10.1016/j.apmt.2019.06.006.

(47) Cotin, G.; Perton, F.; Petit, C.; Sall, S.; Kiefer, C.; Begin, V.; Pichon, B.; Lefevre, C.; Mertz, D.; Greneche, J.-M.; Begin-Colin, S. Harnessing Composition of Iron Oxide Nanoparticle: Impact of Solvent-Mediated Ligand–Ligand Interaction and Competition between Oxidation and Growth Kinetics. *Chem. Mater.* **2020**, *32* (21), 9245–9259. https://doi.org/10.1021/acs.chemmater.0c03041.

(48) Cotin, G.; Kiefer, C.; Perton, F.; Ihiawakrim, D.; Blanco-Andujar, C.; Moldovan, S.; Lefevre, C.; Ersen, O.; Pichon, B.; Mertz, D.; Bégin-Colin, S. Unravelling the

View Article Online
DOI: 10.1039/D4NR01388C

Thermal Decomposition Parameters for The Synthesis of Anisotropic Iron Oxide Nanoparticles. *Nanomaterials* **2018**, *8* (11), 881. https://doi.org/10.3390/nano8110881.

(49) Garaio, E.; Collantes, J. M.; Plazaola, F.; Garcia, J. A.; Castellanos-Rubio, I. A Multifrequency Eletromagnetic Applicator with an Integrated AC Magnetometer for Magnetic Hyperthermia Experiments. *Meas. Sci. Technol.* **2014**, *25* (11), 115702. https://doi.org/10.1088/0957-0233/25/11/115702.

(50) Périgo, E. A.; Hemery, G.; Sandre, O.; Ortega, D.; Garaio, E.; Plazaola, F.; Teran, F. J. Fundamentals and Advances in Magnetic Hyperthermia. *Applied Physics Reviews* **2015**, *2* (4), 041302. https://doi.org/10.1063/1.4935688.

(51) Baaziz, W.; Pichon, B. P.; Fleutot, S.; Liu, Y.; Lefevre, C.; Greneche, J.-M.; Toumi, M.; Mhiri, T.; Begin-Colin, S. Magnetic Iron Oxide Nanoparticles: Reproducible Tuning of the Size and Nanosized-Dependent Composition, Defects, and Spin Canting. *The Journal of Physical Chemistry C* **2014**, *118* (7), 3795–3810. https://doi.org/10.1021/jp411481p.

(52) Cotin, G.; Blanco-Andujar, C.; Perton, F.; Asín, L.; de la Fuente, J. M.; Reichardt, W.; Schaffner, D.; Ngyen, D.-V.; Mertz, D.; Kiefer, C.; Meyer, F.; Spassov, S.; Ersen, O.; Chatzidakis, M.; Botton, G. A.; Hénoumont, C.; Laurent, S.; Greneche, J.-M.; Teran, F. J.; Ortega, D.; Felder-Flesch, D.; Begin-Colin, S. Unveiling the Role of Surface, Size, Shape and Defects of Iron Oxide Nanoparticles for Theranostic Applications. *Nanoscale* **2021**, *13* (34), 14552–14571. https://doi.org/10.1039/D1NR03335B.

(53) Dalmônico, G. M. L.; Ihiawakrim, D.; Ortiz, N.; Barreto Junior, A. G.; Curitiba Marcellos, C. F.; Farina, M.; Ersen, O.; Rossi, A. L. Live Visualization of the Nucleation and Growth of Needle-Like Hydroxyapatite Crystals in Solution by In Situ TEM. *Crystal Growth & Design* **2022**, *22* (8), 4828–4837. https://doi.org/10.1021/acs.cgd.2c00296.

(54) Ramnarain, V.; Georges, T.; Ortiz Peña, N.; Ihiawakrim, D.; Longuinho, M.; Bulou, H.; Gervais, C.; Sanchez, C.; Azaïs, T.; Ersen, O. Monitoring of CaCO3 Nanoscale Structuration through Real-Time Liquid Phase Transmission Electron Microscopy and Hyperpolarized NMR. *J. Am. Chem. Soc.* **2022**, *144* (33), 15236–15251. https://doi.org/10.1021/jacs.2c05731.

(55) Sidhoum, C.; Constantin, D.; Ihiawakrim, D.; Lenertz, M.; Bizien, T.; Sanchez, C.; Ersen, O. Shedding Light on the Birth of Hybrid Perovskites: A Correlative Study by In Situ Electron Microscopy and Synchrotron-Based X-Ray Scattering. *Chem. Mater.* **2023**, *35* (19), 7943–7956. https://doi.org/10.1021/acs.chemmater.3c01167.

(56) ALOthman, Z. A. A Review: Fundamental Aspects of Silicate Mesoporous Materials. *Materials* **2012**, *5* (12), 2874–2902. https://doi.org/10.3390/ma5122874.

(57) Kesse, X.; Adam, A.; Begin-Colin, S.; Mertz, D.; Larquet, E.; Gacoin, T.; Maurin, I.; Vichery, C.; Nedelec, J.-M. Elaboration of Superparamagnetic and Bioactive Multicore–Shell Nanoparticles (γ-Fe $_2$ O $_3$ @SiO $_2$ -CaO): A Promising Material for Bone Cancer Treatment. *ACS Applied Materials & Interfaces* **2020**, *12* (42), 47820–47830. https://doi.org/10.1021/acsami.0c12769.

(58) Weinstein, J. S.; Varallyay, C. G.; Dosa, E.; Gahramanov, S.; Hamilton, B.; Rooney, W. D.; Muldoon, L. L.; Neuwelt, E. A. Superparamagnetic Iron Oxide Nanoparticles: Diagnostic Magnetic Resonance Imaging and Potential Therapeutic Applications in Neurooncology and Central Nervous System

Inflammatory Pathologies, a Review. *J Cereb Blood Flow Metab* **2010**, *30* (1), 15–35. https://doi.org/10.1038/jcbfm.2009.192.

(59) Basly, B.; Felder-Flesch, D.; Perriat, P.; Billotey, C.; Taleb, J.; Pourroy, G.; Begin-Colin, S. Dendronized Iron Oxide Nanoparticles as Contrast Agents for MRI. *Chem. Commun.* **2010**, *46* (6), 985–987. https://doi.org/10.1039/B920348F.

(60) Walter, A.; Billotey, C.; Garofalo, A.; Ulhaq-Bouillet, C.; Lefèvre, C.; Taleb, J.; Laurent, S.; Vander Elst, L.; Muller, R. N.; Lartigue, L.; Gazeau, F.; Felder-Flesch, D.; Begin-Colin, S. Mastering the Shape and Composition of Dendronized Iron Oxide Nanoparticles To Tailor Magnetic Resonance Imaging and Hyperthermia. *Chemistry of Materials* **2014**, *26* (18), 5252–5264. https://doi.org/10.1021/cm5019025.

(61) Wang, W.; Li, F.; Li, S.; Hu, Y.; Xu, M.; Zhang, Y.; Khan, M. I.; Wang, S.; Wu, M.; Ding, W.; Qiu, B. M2 Macrophage-Targeted Iron Oxide Nanoparticles for Magnetic Resonance Image-Guided Magnetic Hyperthermia Therapy. *Journal of Materials Science & Technology* **2021**, *81*, 77–87. https://doi.org/10.1016/j.jmst.2020.11.058.

(62) Mille, N.; De Masi, D.; Faure, S.; Asensio, J. M.; Chaudret, B.; Carrey, J. Probing Dynamics of Nanoparticle Chains Formation during Magnetic Hyperthermia Using Time-Dependent High-Frequency Hysteresis Loops. *Appl. Phys. Lett.* **2021**, *119* (2). https://doi.org/10.1063/5.0056449.

(63) Martinez-Boubeta, C.; Simeonidis, K.; Makridis, A.; Angelakeris, M.; Iglesias, O.; Guardia, P.; Cabot, A.; Yedra, L.; Estradé, S.; Peiró, F.; Saghi, Z.; Midgley, P. A.; Conde-Leborán, I.; Serantes, D.; Baldomir, D. Learning from Nature to Improve the Heat Generation of Iron-Oxide Nanoparticles for Magnetic Hyperthermia Applications. *Scientific Reports* **2013**, *3* (1). https://doi.org/10.1038/srep01652.

(64) Serantes, D.; Simeonidis, K.; Angelakeris, M.; Chubykalo-Fesenko, O.; Marciello, M.; Morales, M. del P.; Baldomir, D.; Martinez-Boubeta, C. Multiplying Magnetic Hyperthermia Response by Nanoparticle Assembling. *The Journal of Physical Chemistry C* **2014**, *118* (11), 5927–5934. https://doi.org/10.1021/jp410717m.

(65) Adam, A. Nanoplateformes à Base de Silices Mésoporeuses Fonctionnelles Pour l'hyperthermie Magnétique, La Photothermie et La Délivrance d'agents Thérapeutiques. phdthesis, Université de Strasbourg, 2022. http://www.theses.fr/s269276 (accessed 2023-02-09).

(66) J. Wells, S. S. and, D. Ortega, U. Steinhoff, S. Dutz, E. Garaio, O. Sandre, E. Natividad, M. M. Cruz, F. Brero, P. Southern, Q. A. Pankhurst. Challenges and Recommendations for Magnetic Hyperthermia Characterization Measurements. *International Journal of Hyperthermia* **2021**, *38* (1), 447–460. https://doi.org/10.1080/02656736.2021.1892837.

(67) Rosensweig, R. E. Heating Magnetic Fluid with Alternating Magnetic Field. *Journal of Magnetism and Magnetic Materials* **2002**, *252*, 370–374. https://doi.org/10.1016/S0304-8853(02)00706-0.

(68) Gavilán, H.; Rizzo, G. M. R.; Silvestri, N.; Mai, B. T.; Pellegrino, T. Scale-up Approach for the Preparation of Magnetic Ferrite Nanocubes and Other Shapes with Benchmark Performance for Magnetic Hyperthermia Applications. *Nat Protoc* **2023**, *18* (3), 783–809. https://doi.org/10.1038/s41596-022-00779-3.

(69) Stolik, S.; Delgado, J. .; Pérez, A.; Anasagasti, L. Measurement of the Penetration Depths of Red and near Infrared Light in Human "Ex Vivo" Tissues.

Journal of Photochemistry and Photobiology B: Biology **2000**, *57* (2–3), 90–93. https://doi.org/10.1016/S1011-1344(00)00082-8.

(70) Henderson, T. A.; Morries, L. Near-Infrared Photonic Energy Penetration: Can Infrared Phototherapy Effectively Reach the Human Brain? *NDT* **2015**, 2191. https://doi.org/10.2147/NDT.S78182.

(71) Espinosa, A.; Di Corato, R.; Kolosnjaj-Tabi, J.; Flaud, P.; Pellegrino, T.; Wilhelm, C. Duality of Iron Oxide Nanoparticles in Cancer Therapy: Amplification of Heating Efficiency by Magnetic Hyperthermia and Photothermal Bimodal Treatment. *ACS Nano* **2016**, *10* (2), 2436–2446. https://doi.org/10.1021/acsnano.5b07249.

(72) Sadat, M. E.; Kaveh Baghbador, M.; Dunn, A. W.; Wagner, H. P.; Ewing, R. C.; Zhang, J.; Xu, H.; Pauletti, G. M.; Mast, D. B.; Shi, D. Photoluminescence and Photothermal Effect of Fe_3O_4 Nanoparticles for Medical Imaging and Therapy. *Appl. Phys. Lett.* **2014**, *105* (9), 091903. https://doi.org/10.1063/1.4895133.

(73) Bertuit, E.; Benassai, E.; Mériguet, G.; Greneche, J.-M.; Baptiste, B.; Neveu, S.; Wilhelm, C.; Abou-Hassan, A. Structure–Property–Function Relationships of Iron Oxide Multicore Nanoflowers in Magnetic Hyperthermia and Photothermia. *ACS Nano* **2022**, *16* (1), 271–284. https://doi.org/10.1021/acsnano.1c06212.

(74) Hergt, R.; Dutz, S. Magnetic Particle Hyperthermia—biophysical Limitations of a Visionary Tumour Therapy. *Journal of Magnetism and Magnetic Materials* **2007**, *311* (1), 187–192. https://doi.org/10.1016/j.jmmm.2006.10.1156.

(75) Clerc, P.; Jeanjean, P.; Hallali, N.; Gougeon, M.; Pipy, B.; Carrey, J.; Fourmy, D.; Gigoux, V. Targeted Magnetic Intra-Lysosomal Hyperthermia Produces Lysosomal Reactive Oxygen Species and Causes Caspase-1 Dependent Cell Death. *Journal of Controlled Release* **2018**, *270*, 120–134. https://doi.org/10.1016/j.jconrel.2017.11.050.

(76) Croissant, J. G.; Fatieiev, Y.; Khashab, N. M. Degradability and Clearance of Silicon, Organosilica, Silsesquioxane, Silica Mixed Oxide, and Mesoporous Silica Nanoparticles. *Adv. Mater.* **2017**, *29* (9), 1604634. https://doi.org/10.1002/adma.201604634.

(77) Brauchle, E.; Thude, S.; Brucker, S. Y.; Schenke-Layland, K. Cell Death Stages in Single Apoptotic and Necrotic Cells Monitored by Raman Microspectroscopy. *Sci Rep* **2014**, *4* (1), 1–9. https://doi.org/10.1038/srep04698.

(78) Creixell, M.; Bohórquez, A. C.; Torres-Lugo, M.; Rinaldi, C. EGFR-Targeted Magnetic Nanoparticle Heaters Kill Cancer Cells without a Perceptible Temperature Rise. *ACS Nano* **2011**, *5* (9), 7124–7129. https://doi.org/10.1021/nn201822b.

(79) Sanchez, C.; El Hajj Diab, D.; Connord, V.; Clerc, P.; Meunier, E.; Pipy, B.; Payré, B.; Tan, R. P.; Gougeon, M.; Carrey, J.; Gigoux, V.; Fourmy, D. Targeting a G-Protein-Coupled Receptor Overexpressed in Endocrine Tumors by Magnetic Nanoparticles To Induce Cell Death. *ACS Nano* **2014**, *8* (2), 1350–1363. https://doi.org/10.1021/nn404954s.

(80) Xia, T.; Kovochich, M.; Liong, M.; Meng, H.; Kabehie, S.; George, S.; Zink, J. I.; Nel, A. E. Polyethyleneimine Coating Enhances the Cellular Uptake of Mesoporous Silica Nanoparticles and Allows Safe Delivery of SiRNA and DNA Constructs. *ACS Nano* **2009**, *3* (10), 3273–3286. https://doi.org/10.1021/nn900918w.

(81) Kar, M.; Tiwari, N.; Tiwari, M.; Lahiri, M.; Gupta, S. S. Poly-L-Arginine Grafted Silica Mesoporous Nanoparticles for Enhanced Cellular Uptake and Their Application in DNA Delivery and Controlled Drug Release. *Particle & Particle*

Systems Characterization **2013**, *30* (2), 166–179. https://doi.org/10.1002/ppsc.201200089.

(82) Yu, M.; Jambhrunkar, S.; Thorn, P.; Chen, J.; Gu, W.; Yu, C. Hyaluronic Acid Modified Mesoporous Silica Nanoparticles for Targeted Drug Delivery to CD44-Overexpressing Cancer Cells. *Nanoscale* **2013**, *5* (1), 178–183. https://doi.org/10.1039/C2NR32145A.